J. Fluid Mech. (2002), *vol.* 465, *pp.* 99–130.
DOI: 10.1017/S0022112002008996 Printed in the United Kingdom

Navier–Stokes solutions of unsteady separation induced by a vortex

By A. V. OBABKO AND K. W. CASSEL

Fluid Dynamics Research Center, Mechanical, Materials and Aerospace Engineering Department, Illinois Institute of Technology, Chicago, IL 60616, USA

(Received 18 June 2001 and in revised form 15 February 2002)

Numerical solutions of the unsteady Navier–Stokes equations are considered for the flow induced by a thick-core vortex convecting along a surface in a two-dimensional incompressible flow. The presence of the vortex induces an adverse streamwise pressure gradient along the surface that leads to the formation of a secondary recirculation region followed by a narrow eruption of near-wall fluid in solutions of the unsteady boundary-layer equations. The locally thickening boundary layer in the vicinity of the eruption provokes an interaction between the viscous boundary layer and the outer inviscid flow. Numerical solutions of the Navier–Stokes equations show that the interaction occurs on two distinct streamwise length scales depending upon which of three Reynolds-number regimes is being considered. At high Reynolds numbers, the spike leads to a small-scale interaction; at moderate Reynolds numbers, the flow experiences a large-scale interaction followed by the small-scale interaction due to the spike; at low Reynolds numbers, large-scale interaction occurs, but there is no spike or subsequent small-scale interaction. The large-scale interaction is found to play an essential role in determining the overall evolution of unsteady separation in the moderate-Reynolds-number regime; it accelerates the spike formation process and leads to formation of secondary recirculation regions, splitting of the primary recirculation region into multiple corotating eddies and ejections of near-wall vorticity. These eddies later merge prior to being lifted away from the surface and causing detachment of the thick-core vortex.

1. Introduction

The interest in unsteady separation stems from its ubiquitous nature in applications involving high-Reynolds-number surface-bounded flows and the central role that it plays in many of these applications. Essentially, any unsteady high-Reynolds-number flow in which a boundary layer is subject to an adverse streamwise pressure gradient can lead to unsteady separation involving formation of a recirculation region and an intense eruption of near-wall vorticity. Described by Doligalski, Smith & Walker (1994) as 'one of the most important unsolved problems of fluid dynamics', applications of unsteady separation include formation and detachment of the dynamic-stall vortex on pitching airfoils and helicopter blades, the turbulence generation mechanism near solid surfaces, the flow upstream of surface-mounted obstacles, and the flow through various portions of turbine and compressor passages and branching pipes (see, for example, Smith *et al.* 1991; Doligalski *et al.* 1994; Seal *et al.* 1995; Smith & Walker 1995; Seal, Smith & Rockwell 1997).

From the point of view of the unsteady boundary-layer equations, unsteady separ-

ation is defined as the onset of a finite-time singularity. According to the Moore–Rott–Sears (MRS) model of unsteady separation articulated by Sears & Telionis (1975), this singularity occurs along the zero vorticity line and moves with the local flow velocity. The boundary-layer equations are an exact subset of the Navier–Stokes equations as $Re \to \infty$, and a singularity indicates that boundary-layer fluid has penetrated much farther from the wall than allowed for by the boundary-layer approximation. In other words, the near-wall boundary-layer vorticity is ejected an infinite distance from the surface, on the boundary-layer scale, in order to overcome the vanishing boundary-layer thickness, which is $O(Re^{-1/2})$. Consequently, the formation of the singularity may be thought of as the first time at which the assumption that the boundary-layer remains thin and attached breaks down, and the erupting boundary layer has a significant influence on the external inviscid flow with the onset of a viscous–inviscid interaction.

The basic eruptive phenomenon and boundary-layer singularity were first observed by Van Dommelen (1981) and Van Dommelen & Shen (1980, 1982). Using the Lagrangian formulation of the unsteady two-dimensional incompressible boundary-layer equations, they have shown that a singularity forms in the non-interactive boundary-layer solution on a circular cylinder that is impulsively started from rest. In the latter stages of the numerical calculations, the boundary layer focuses into a narrow region that forms on the upstream side of the recirculation zone; as a fluid particle at the separation point is rapidly compressed in the streamwise direction, it elongates in the direction normal to the wall. This elongation of the fluid particle in the normal direction leads to growth of a sharp spike in the displacement thickness as the boundary layer erupts away from the surface.

The high-Reynolds-number asymptotic structure of unsteady separation is summarized schematically in figure 1, with each tier representing a subsequent asymptotic stage and time moving from left to right. Each stage is governed by its own reduced set of the Navier–Stokes equations. The bottom tier corresponds to the non-interactive boundary-layer stage computed by Van Dommelen (1981) which terminates in a singularity at $t = t_s$. Van Dommelen & Shen (1982) and Elliott, Cowley & Smith (1983) have obtained an analytical solution of the terminal singular structure for two-dimensional incompressible flows, denoted by I in figure 1. It was shown that as the flow evolves toward the singularity, the boundary layer bifurcates into two passive shear layers above and below an intermediate vorticity-depleted region, i.e. a region in which the velocity is nearly constant surrounding the zero-vorticity line. As the boundary layer approaches the singularity time t_s, this intermediate region thins in the streamwise direction and grows rapidly in the direction normal to the surface at a rate proportional to $(t_s - t)^{-1/4}$, forming a narrow spike. An important characteristic of the terminal solution is its independence from the external adverse pressure gradient that initiated the separation process. Consequently, the terminal boundary-layer solution has been regarded as a generic structure that applies to most cases of unsteady boundary-layer separation in two-dimensional incompressible flows (Cowley, Van Dommelen & Lam 1990). Indeed, solutions for the unsteady boundary-layer flow in a curved pipe (Lam 1988), rectilinear vortex-induced separation (Peridier, Smith & Walker 1991*a*) and flow past the leading edge of a thin airfoil (Degani, Li & Walker 1996) terminate in the non-interactive boundary-layer singularity at a finite time.

The separation singularity develops in the non-interactive boundary-layer solution as a result of a prescribed mainstream adverse pressure gradient and indicates that new physics must become important just prior to the onset of the singularity. As the

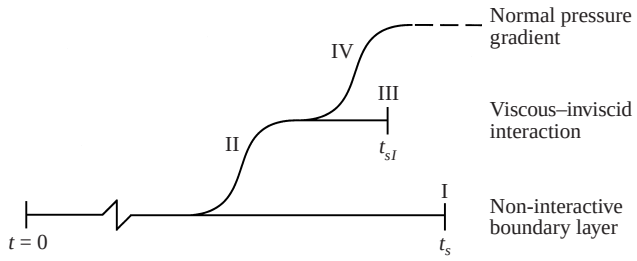

FIGURE 1. Schematic of the initial asymptotic structure of unsteady separation.

spike grows, the external flow begins to respond, leading to interaction between the viscous boundary layer and the inviscid outer flow. Elliott *et al.* (1983) formulated the first interactive stage that starts when $t_s - t = O(Re^{-2/11})$, denoted by II in figure 1, and leads to the second stage of unsteady separation (the second tier in figure 1). The initial condition for the first interactive stage is the terminal boundary-layer solution; therefore, this asymptotic theory is predicated on the assumption that the explosively growing spike is a precursor to the viscous–inviscid interaction. Cassel, Smith & Walker (1996) have obtained a numerical solution of this stage in Lagrangian coordinates that exhibits a high-frequency inviscid instability resulting in an immediate breakdown of the first interactive stage. These results suggest that some other physical influence may become important prior to the time scale over which the first interactive stage acts.

Peridier, Smith & Walker (1991*b*) used an alternative approach to account for viscous–inviscid interaction, the so-called interacting boundary-layer theory. They computed the unsteady separation induced by a rectilinear vortex at large finite Reynolds numbers using Lagrangian coordinates. Apparently unencumbered by the instability of Cassel *et al.* (1996), the solution broke down in an interactive singularity in the streamwise pressure gradient and wall shear distribution, denoted by III in figure 1, which is consistent with the predictions by Smith (1988). Note that the interactive-singularity time t_{sI} was found to be prior to the terminal-solution-singularity time t_s, i.e. $t_{sI} < t_s$.

In order to relieve the interacting boundary-layer singularity, the next stage of unsteady separation was proposed by Hoyle, Smith & Walker (1991) and considered in more detail by Li *et al.* (1998). This stage, using the interacting boundary-layer equations as its starting point, is characterized by the onset of local effects caused by an increasing normal pressure gradient, which is zero to leading order in the non-interactive and first interactive stages. Normal pressure gradient effects are associated with the formation of a critical layer near an inflection point in the streamwise velocity profiles and result in vortex wind-up near an extremum in the wall pressure. This normal pressure gradient stage is represented by the third tier in figure 1.

In summary, the theory that has been developed for describing the unsteady separation process has arisen beginning with two reduced sets of equations: (i) the unsteady non-interacting boundary-layer equations, which leads to the first interactive stage, and (ii) unsteady interacting boundary-layer theory. Whereas the first approach is exact as $Re \to \infty$, the second approach applies for large finite Reynolds numbers. The expectation has been that the theory arising from the non-interacting boundary-layer equations as a starting point is the limiting form as $Re \to \infty$ of the theory arising from interacting boundary-layer theory. However, the work of Cassel *et al.* (1996) cast into doubt whether the first interactive stage is consistent within such a

framework. It was suggested by Cassel (2000) that this may be due to the presence of a large-scale interaction that occurs prior to spike formation and, therefore, the small-scale interaction described by the first interactive stage.

Numerical investigations of unsteady separation typically have been considered from two points of view, namely (i) solutions of subsets of the Navier–Stokes equations corresponding to the limit problem as $Re \to \infty$, or (ii) solutions of the full Navier–Stokes equations. The first approach, as summarized above, has provided a great deal of insight into the physical processes involved in unsteady separation. Solutions of the full Navier–Stokes equations have the advantage that they do not make any inherent physical assumptions about the flow; however, they are typically carried out at relatively low Reynolds numbers owing to the increased resolution required as the Reynolds number is increased. As a result, solutions obtained using these two approaches generally exhibit somewhat different behaviour. In particular, the Reynolds numbers considered in most solutions of the Navier–Stokes equations typically have not been large enough to observe the sharp spike that occurs in unsteady separation at high Reynolds numbers (see, for example, Orlandi 1990; Koumoutsakos & Leonard 1995; Ghosh Choudhuri & Knight 1996). A recent study by Brinckman & Walker (2001), however, does reveal formation of a spike in a Navier–Stokes calculation of the flow induced by a vortex.

In order to further bridge the gap between solutions of the Navier–Stokes equations at relatively low Reynolds numbers and solutions corresponding to the limit problem, high-resolution numerical solutions of the unsteady Navier–Stokes equations have been obtained for the flow induced by a thick-core vortex above an infinite plane wall. The thick-core vortex is one in which the vorticity is distributed throughout the vortex (Batchelor 1967), in contrast to the rectilinear vortex in which the vorticity is entirely focused in the centre of the vortex.

Detailed results for the case with $Re = 10^5$ are given in Cassel (2000), where the objective was to identify the three initial asymptotic stages of unsteady separation (see figure 1) within the context of a Navier–Stokes solution at a large, but finite, Reynolds number. The numerical results for $Re = 10^5$ are consistent with this sequence of events except that interaction has been found to begin much earlier than allowed for by the high-Reynolds-number asymptotic theory. Based on these results, it has been hypothesized that there is a moderate-Reynolds-number regime in which the strong outflows that develop within the boundary layer cause a large-scale interaction prior to spike formation. Rapid growth of the spike then leads to a small-scale interaction as in the high-Reynolds-number regime governed by the asymptotic theory. These forms of interaction occur over two distinct streamwise scales depending upon the Reynolds number of the flow.

One purpose of the present investigation is to consider a range of Reynolds numbers in order to determine its effect upon the large-scale and small-scale interaction. It is found that in terms of the viscous–inviscid interaction, there are three Reynolds-number regimes. In the high-Reynolds-number regime, the flow is governed by the asymptotic limit problem and only small-scale interaction occurs as a result of the erupting spike. In the moderate-Reynolds-number regime, a large-scale interaction precedes the spike formation and the subsequent small-scale interaction. At low Reynolds numbers, the large-scale interaction occurs just as in the moderate-Reynolds-number regime; however, no spike forms, and there is no small-scale interaction. An additional purpose is to determine the post-eruptive behaviour that ultimately leads to a significant interaction with the thick-core vortex and its detachment.

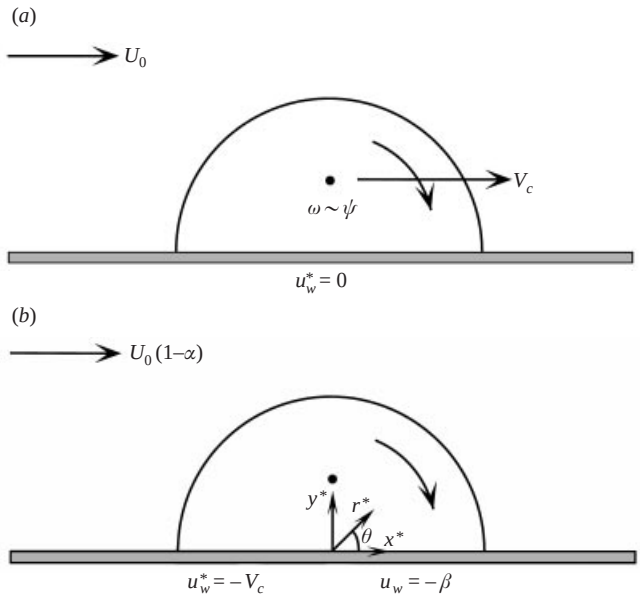

FIGURE 2. Schematic of the thick-core vortex. (*a*) Fixed frame of reference, (*b*) frame of reference moving with the vortex.

2. Problem formulation and numerical methods

2.1. *Inviscid solution for the thick-core vortex*

The inviscid flow due to the thick-core vortex above a plane wall is described by Batchelor (1967) and consists of a semi-circular vortex, in which the vorticity is proportional to the streamfunction, surrounded by the irrotational flow due to a circular cylinder in a uniform flow with speed U_0. The thick-core vortex is shown schematically in figure 2. As shown by Batchelor, the dimensional vorticity and streamfunction in the core of the vortex are related by $\omega^* = k^2\psi^*$ and $\psi^* \sim J_1(kr^*)\sin\theta$, where k is a constant, J_1 is the first-order Bessel function of the first kind, and (r^*, θ) are cylindrical coordinates. Note that here and throughout, dimensional variables are denoted with an asterisk. For convenience, the radius of the non-zero vorticity core is set equal to e, the base of the natural logarithm, and k is chosen such that $J_1(ke) = 0$ in order to match the zero value of the streamfunction due to the irrotational flow around a cylinder at the core boundary $r^* = e$. Letting $\lambda = ke$ be equal to the first zero of J_1 corresponds to the simplest case of a single-cell vortex.

The vortex has a velocity V_c relative to the wall owing to its self-induced flow and the free-stream velocity U_0. Note that if placed in a stagnant fluid, i.e. $U_0 = 0$, a vortex with negative sign rotation, as shown in figure 2, will convect in the negative x-direction ($V_c < 0$) owing to its self-induced velocity. As in Doligalski & Walker (1984) and Degani, Walker & Smith (1998), the following parameters are defined in order to characterize the speed of the vortex

$$\alpha = \frac{V_c}{U_0}, \quad \beta = \frac{\alpha}{1-\alpha}, \tag{2.1a,b}$$

where α is the fractional convection rate of the vortex relative to the free-stream velocity, and β is the non-dimensional wall speed in a frame of reference moving with the vortex. The case with $\beta = 0$ ($\alpha = 0$) corresponds to a vortex with sufficient

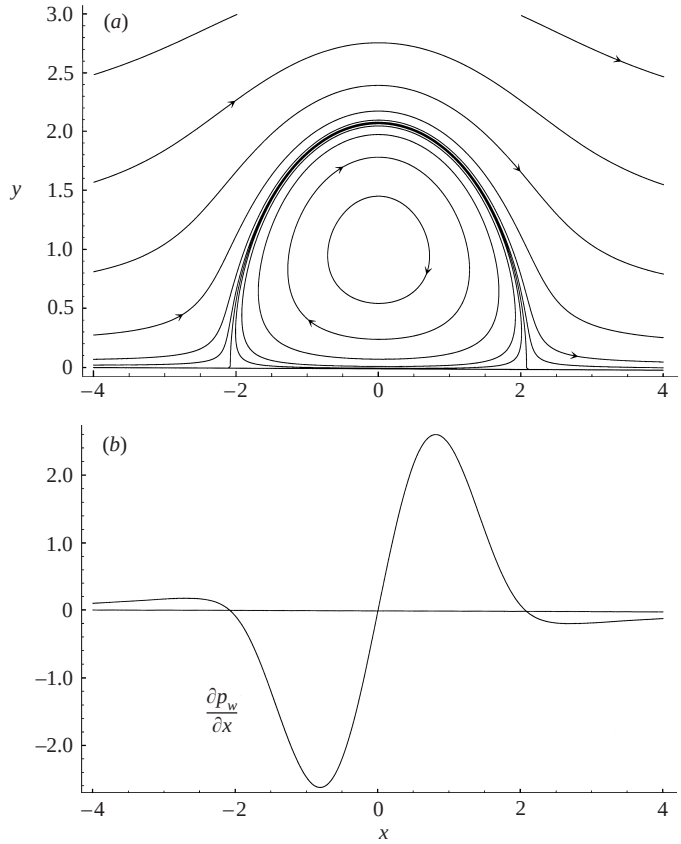

FIGURE 3. Inviscid solution for the thick-core vortex. (*a*) Streamlines, (*b*) streamwise pressure gradient along the surface.

self-induced velocity to exactly balance the free-stream velocity and remain stationary relative to the wall. The influence of a moving wall is considered in Obabko & Cassel (2002). Note that the case with $\beta \to -1$ ($\alpha \to \infty$) corresponds to a vortex propagating in a stagnant fluid, i.e. $U_0 = 0$. This case was investigated by Walker (1978) and Peridier *et al.* (1991*a*, *b*), who considered the unsteady boundary-layer induced by a rectilinear vortex above an infinite plane wall.

Defining r_0 to be the normal distance from the surface to the centre of the vortex, and taking r_0 to be the characteristic length and the velocity at infinity, $U_0(1-\alpha)$, to be the characteristic velocity, it is shown in Cassel (2000) that the non-dimensional streamfunction in cylindrical coordinates in a frame of reference moving with the vortex is

$$\psi_0(r,\theta) = \left[r - \frac{1}{r}\left(\frac{e}{r_0}\right)^2\right]\sin\theta, \quad r > \frac{e}{r_0}, \tag{2.2a}$$

$$\psi_0(r,\theta) = \frac{2}{r_0}\frac{J_1(kr_0 r)}{kJ_0(\lambda)}\sin\theta, \quad r \leqslant \frac{e}{r_0}, \tag{2.2b}$$

where kr_0 is the first zero of the derivative of the Bessel function of the first kind. The resulting inviscid streamlines and streamwise pressure gradient along the surface are shown in figures 3(*a*) and 3(*b*), respectively. The stagnation points on the wall are

located at $x = \pm 2.0811$, where x is the coordinate along the wall, non-dimensionalized using r_0, with the origin centred beneath the vortex. The pressure gradient is adverse between the origin and the left stagnation point with respect to the local flow direction in the lower portion of the vortex, which is from right to left. Equations (2.2) prescribe the inviscid solution for the thick-core vortex above an infinite plane wall and provide the initial condition for the impulsively-started Navier–Stokes calculations.

2.2. *Navier–Stokes formulation*

The Navier–Stokes equations in Cartesian coordinates are non-dimensionalized as above using r_0 for the characteristic length and $U_0(1-\alpha)$ for the characteristic velocity. In this investigation, the two-dimensional incompressible Navier–Stokes equations are calculated using the vorticity–streamfunction formulation with the vorticity transport equation

$$\frac{\partial \omega}{\partial t} + u\frac{\partial \omega}{\partial x} + v\frac{\partial \omega}{\partial y} = \frac{1}{Re}\left[\frac{\partial^2 \omega}{\partial x^2} + \frac{\partial^2 \omega}{\partial y^2}\right], \tag{2.3}$$

where the Reynolds number is defined by $Re = U_0(1-\alpha)r_0/\nu$, and a Poisson equation for the streamfunction

$$\frac{\partial^2 \psi}{\partial x^2} + \frac{\partial^2 \psi}{\partial y^2} = -\omega. \tag{2.4}$$

The streamfunction is defined by $u = \partial\psi/\partial y$, $v = -\partial\psi/\partial x$.

The flow is impulsively started at $t = 0$ using the inviscid solution for the thick-core vortex (2.2) expressed in Cartesian coordinates (see Cassel 2000) as the initial condition. Note that the centre of the vortex is initially located at $x = 0$, $y = 1$. The initial vorticity distribution can be obtained by substituting the expression for the streamfunction (2.2) into the Poisson equation (2.4) written in cylindrical coordinates to give

$$\omega_0(r, \theta) = 0, \quad r > e/r_0, \tag{2.5a}$$

$$\omega_0(r, \theta) = (kr_0)^2 \psi_0(r, \theta), \quad r \leqslant e/r_0, \tag{2.5b}$$

at $t = 0$.

The boundary conditions on the streamfunction, velocity components and vorticity at the wall and as $y \to \infty$ are

$$\psi = 0, \quad u = -\beta, \quad v = 0 \quad \text{at} \quad y = 0, \tag{2.6a}$$

$$\psi \to y, \quad u \to 1, \quad v \to 0, \quad \omega \to 0 \quad \text{as} \quad y \to \infty. \tag{2.6b}$$

At upstream and downstream infinity the flow is fully developed and plane parallel, and as shown in Cassel (2000), the streamwise velocity, streamfunction and vorticity are as follows

$$u = (1 + \beta)\mathrm{erf}(\eta) - \beta, \quad |x| \to \infty, \tag{2.7a}$$

$$\psi = 2\sqrt{\frac{t}{Re}}\left\{(1 + \beta)\left[\eta\,\mathrm{erf}(\eta) - \frac{1}{\sqrt{\pi}}(1 - \mathrm{e}^{-\eta^2})\right] - \beta\eta\right\}, \quad |x| \to \infty, \tag{2.7b}$$

$$\omega = -\frac{\partial u}{\partial y} = -\frac{1 + \beta}{\sqrt{\pi}}\sqrt{\frac{Re}{t}}\mathrm{e}^{-\eta^2}, \quad |x| \to \infty, \tag{2.7c}$$

where $\eta = \frac{1}{2}y(Re/t)^{1/2}$.

In order to map the semi-infinite physical domain into a finite computational

domain and to focus grid points in regions having large gradients, the following coordinate transformations are used

$$\hat{x} = \frac{2}{\pi}\arctan\left(\frac{x - x_0}{a}\right), \quad \hat{y} = \frac{2}{\pi}\arctan\left(\frac{y}{b}\right). \tag{2.8a, b}$$

This transformation maps $x \to \infty$ to $\hat{x} = 1$ and $x \to -\infty$ to $\hat{x} = -1$, and concentrates grid points near $x = x_0$, the streamwise location of the eruption, and $y = 0$, the surface. The parameters a and b determine the degree of focusing of grid points, with smaller values increasing the resolution in the desired regions. Applying these transformations to the vorticity transport equation (2.3) gives

$$\frac{\partial \omega}{\partial t} = R(\hat{x})\frac{\partial^2 \omega}{\partial \hat{x}^2} + S(\hat{x})\frac{\partial^2 \omega}{\partial \hat{y}^2} + G(\hat{x}, \hat{y})\frac{\partial \omega}{\partial \hat{x}} + H(\hat{x}, \hat{y})\frac{\partial \omega}{\partial \hat{y}}, \tag{2.9a}$$

where

$$R(\hat{x}) = \frac{1}{Re}\Gamma_x^2(\hat{x}), \tag{2.9b}$$

$$S(\hat{y}) = \frac{1}{Re}\Gamma_y^2(\hat{y}), \tag{2.9c}$$

$$G(\hat{x}, \hat{y}) = \frac{1}{Re}\Gamma_x(\hat{x})\Gamma_x'(\hat{x}) - \Gamma_x(\hat{x})u(\hat{x}, \hat{y}), \tag{2.9d}$$

$$H(\hat{x}, \hat{y}) = \frac{1}{Re}\Gamma_y(\hat{y})\Gamma_y'(\hat{y}) - \Gamma_y(\hat{y})v(\hat{x}, \hat{y}). \tag{2.9e}$$

Applying the transformations to the Poisson equation for the streamfunction (2.4) gives

$$A(\hat{x})\frac{\partial^2 \psi}{\partial \hat{x}^2} + B(\hat{x})\frac{\partial \psi}{\partial \hat{x}} + C(\hat{y})\frac{\partial^2 \psi}{\partial \hat{y}^2} + D(\hat{y})\frac{\partial \psi}{\partial \hat{y}} = E(\hat{x}, \hat{y}), \tag{2.10a}$$

where

$$A(\hat{x}) = \Gamma_x^2(\hat{x}), \quad B(\hat{x}) = \Gamma_x(\hat{x})\Gamma_x'(\hat{x}), \tag{2.10b, c}$$

$$C(\hat{y}) = \Gamma_y^2(\hat{y}), \quad D(\hat{y}) = \Gamma_y(\hat{y})\Gamma_y'(\hat{y}), \tag{2.10d, e}$$

$$E(\hat{x}, \hat{y}) = -\omega(\hat{x}, \hat{y}). \tag{2.10f}$$

The initial condition and boundary conditions (2.6) and (2.7) are likewise transformed into the computational coordinates $(\hat{x}, \hat{y})$. In the above equations, the Γ coefficients are given by

$$\Gamma_x(\hat{x}) = \frac{1}{\pi a}\left[1 + \cos(\pi\hat{x})\right], \tag{2.11a}$$

$$\Gamma_y(\hat{y}) = \frac{1}{\pi b}\left[1 + \cos(\pi\hat{y})\right], \tag{2.11b}$$

and a prime denotes differentiation with respect to the appropriate independent variable.

2.3. *Numerical methods*

In order to advance the numerical solution of the vorticity–streamfunction formulation of the Navier–Stokes equations forward in time, an iteration between the vorticity and streamfunction equations is carried out at each time step until convergence is obtained. The vorticity transport equation (2.9) is solved using a factored

ADI algorithm with Crank–Nicolson time marching and upwind–downwind differencing similar to that described by Peridier *et al.* (1991*a*). The algorithm is effective in computing flows that develop large gradients. The boundary condition for the vorticity at the wall ($y = 0$) is obtained using Jensen's method which provides a second-order accurate approximation to the vorticity at the surface obtained from the streamfunction field. Overall, the method is $O(\Delta x \Delta t, \Delta y \Delta t)$ accurate.

The transformed Poisson equation for the streamfunction (2.10) is solved at each iteration using a multigrid algorithm. This algorithm has been developed to solve general two-dimensional linear second-order elliptic equations with variable coefficients. The equation is discretized using second-order accurate central differences. Because a good initial guess for the solution exists, i.e. the solution from the previous time step, the coarse-grid correction is performed using V-cycles until convergence. The restriction and interpolation operators use full weighting and bilinear interpolation, respectively, and relaxation is performed using an ADI iteration. Details of the multigrid algorithm may be found in Obabko (2001).

Note that in the vorticity–streamfunction formulation, where $\psi \sim y$ as $y \to \infty$, it is necessary to truncate the vertical extent of the domain in order for the streamfunction to remain finite throughout the computational domain. Here, a value of $y_{\max} = 10$ has been found to be sufficiently large not to influence the solution.

3. Results

Numerical solutions of the Navier–Stokes equations for the flow induced by the thick-core vortex are given for Reynolds numbers in the range between 10^3 and 10^5. It should be noted that the Reynolds number defined in this investigation is a local Reynolds number, based on the height of the vortex centre above the wall, and would be much larger if based on a global length scale such as the chord length of an airfoil if the thick-core vortex is considered to be a model of the dynamic-stall vortex. All results shown are for a non-dimensional wall speed of $\beta = 0$. This case corresponds to a situation in which the strength of the vortex is such that the self-induced velocity of the vortex in the inviscid solution exactly balances the free-stream velocity, and the vortex remains stationary relative to the surface. The influence of a moving wall is considered in a companion study by Obabko & Cassel (2002).

3.1. *Comparison of Navier–Stokes solutions with theory*

Before describing numerical solutions of the Navier–Stokes equations at finite Reynolds number, it is instructive to consider the limiting case as $Re \to \infty$, namely solutions of the unsteady non-interacting boundary-layer equations. These boundary-layer solutions should compare well with the Navier–Stokes solutions for large finite Reynolds numbers at early times, i.e. until viscous–inviscid interaction begins, and they are indicative of the limiting-Reynolds-number behaviour in unsteady separation. Numerical solutions of the unsteady boundary-layer equations for the flow induced by a thick-core vortex with $\beta = 0$ are given by Cassel (2000). The boundary-layer solution for this case exhibits a recirculation region that begins to form at approximately $t = 0.4$ in response to the adverse pressure gradient imposed by the thick-core vortex. The recirculation region grows and moves in the positive x-direction, which is locally upstream relative to the flow in the portion of the vortex adjacent to the wall. A kink begins to form in the streamlines and vorticity contours on the upstream side of the recirculation region at approximately $t_{spike} = 1.3$ followed by the formation of a very sharp spike that erupts away from the surface and results in a singularity at

Re	Grid	a	b	x_0	$\Delta x_{\min}$	$\Delta y_{\min}$	Δt
1×10^3	513×513	0.80	0.50	-1.00	4.9×10^{-3}	1.5×10^{-3}	5×10^{-4}
3×10^3	513×513	0.50	0.28	-0.83	3.1×10^{-3}	8.4×10^{-4}	5×10^{-4}
1×10^4	1025×513	0.40	0.15	-0.78	1.2×10^{-3}	4.6×10^{-4}	2×10^{-5}
3×10^4	4097×513	0.20	0.09	-0.75	1.5×10^{-4}	2.7×10^{-4}	2×10^{-6}
1×10^5	1025×513	0.10	0.05	-0.55	3.1×10^{-4}	1.5×10^{-4}	2×10^{-6}

TABLE 1. Computational parameters.

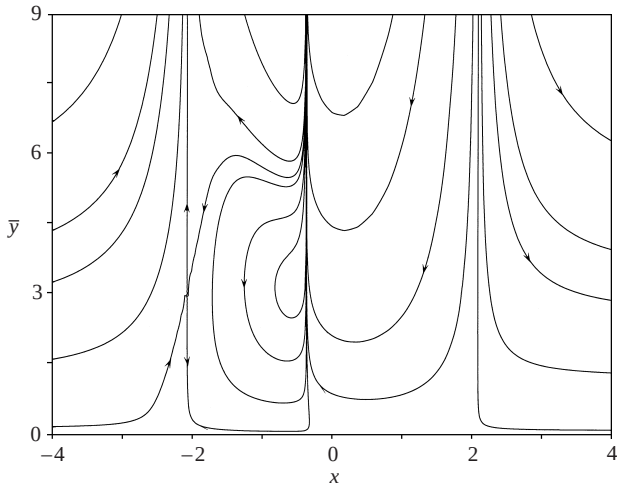

FIGURE 4. Streamlines from a non-interacting boundary-layer calculation, i.e. $Re \to \infty$, at $t_s = 1.402$ (from Cassel 2000).

$t_s = 1.402$ at the streamwise location $x_s = -0.375$, as shown in figure 4. The singularity signals the end of the first asymptotic stage of unsteady separation (the bottom tier in figure 1), and the sharp spike provokes a small-scale viscous–inviscid interaction (the second tier in figure 1). These results for the thick-core vortex are qualitatively the same as those obtained by Peridier *et al.* (1991*a*) for the boundary layer induced by a rectilinear vortex; they only differ in the times at which the above-mentioned events occur.

In this section, the focus is on the flow development, and, in particular, the nature of the viscous–inviscid interaction, up to the approximate time at which the singularity occurs in the boundary-layer calculations, and emphasis is placed on comparison of the Navier–Stokes solutions with the theory of unsteady separation. The flow evolution at later times is described in the next section. Considerable effort has been devoted to ensuring that the results are grid independent and that, when scaled according to the boundary-layer scale, they compare well with solutions of the boundary-layer equations at early times. The results shown have been calculated using the grid sizes, transformation parameters and time steps given in table 1. Note that a and b are small in order to resolve the boundary layer adequately in the region beneath the vortex where unsteady separation occurs. For some of the Reynolds numbers, coarser grids and larger time steps have been used to obtain the solutions during the early stages of the calculations; therefore, table 1 shows the finest grid and the smallest time step for the calculations that produced the results shown for each Reynolds

number. Calculations also have been performed on finer grids in order to ensure that the results shown are grid independent.

In order to determine when viscous–inviscid interaction first begins, the streamwise pressure gradient along the surface is followed with time. To leading order, the streamwise pressure gradient within the boundary layer is imposed by the steady inviscid outer flow, and the normal pressure gradient within the boundary layer is zero during the non-interactive stage of the flow. Therefore, the streamwise pressure gradient along the surface does not change substantially from that given by the inviscid solution (see figure 3*b*) until interaction between the viscous boundary layer and the inviscid outer flow begins. Applying the streamwise momentum equation at the surface and writing in terms of vorticity, the streamwise pressure gradient along the surface may be determined from

$$\left.\frac{\partial p}{\partial x}\right|_{y=0} = -\frac{1}{Re}\Gamma_y(\hat{y})\left.\frac{\partial \omega}{\partial \hat{y}}\right|_{\hat{y}=0}, \tag{3.1}$$

with respect to the transformed normal coordinate.

The evolution of the streamwise pressure gradient along the surface is shown in figure 5 for three Reynolds numbers, $Re = 10^3$, 10^4 and 10^5. In each figure the pressure gradient is shown for a range of times up to $t = 1.0$ in increments of 0.1. In all three cases the pressure gradient is observed to begin changing at a streamwise location in the vicinity of the minimum in pressure gradient, where the streamlines abruptly change direction in order to pass over the recirculation region. For $Re = 10^3$, this occurs within the range $0.6 < t < 0.7$; for $Re = 10^4$, it occurs within the range $0.7 < t < 0.8$; and for $Re = 10^5$, this occurs at approximately $t = 0.8$. The precise time at which interaction begins for the lower Reynolds-number cases is more difficult to determine because it influences the flow over a wider streamwise scale encompassing the minimum in streamwise pressure gradient. However, it is clear that the time at which interaction begins increases as the Reynolds number is increased, and the streamwise extent of the interaction region decreases with increasing Reynolds number.

As discussed in Cassel (2000), the onset of interaction in this way is inconsistent with the asymptotic theory developed for the limiting case $Re \to \infty$, which assumes that it is the rapidly growing spike (see figure 4) that initiates interaction. In the boundary-layer results for the thick-core vortex, the spike does not begin to form until approximately $t_{spike} = 1.3$. In light of this, the interaction that begins between $0.6 \leqslant t \leqslant 0.8$ in the Navier–Stokes solutions for the Reynolds numbers considered will be referred to as a large-scale interaction owing to the larger streamwise scale over which it acts. The interaction that is then induced by the rapidly growing spike at later times will be referred to as a small-scale interaction.

For comparison with the boundary-layer solution at the singularity time $t_s = 1.402$ (figure 4), instantaneous streamlines are given at $t = 1.4$ for $Re = 10^3$ and 10^4 and $t = 1.3$ for $Re = 10^5$ in figure 6. The normal scales in each figure are chosen such that the physical scale y matches the boundary-layer scale $\bar{y}$ in figure 4 according to $y = Re^{-1/2}\bar{y}$. The physical and boundary-layer scales are shown on the left and right vertical axes, respectively. Note that results for $Re = 10^5$ are not shown at $t = 1.4$ owing to the presence of multiple eddies and spikes in a narrow streamwise region that render the flow field very complex and difficult to interpret on the wide streamwise scale shown here. The Navier–Stokes results for $Re = 10^5$ and 10^4 exhibit the rapidly growing spike as in the boundary-layer results, but with increasing streamwise

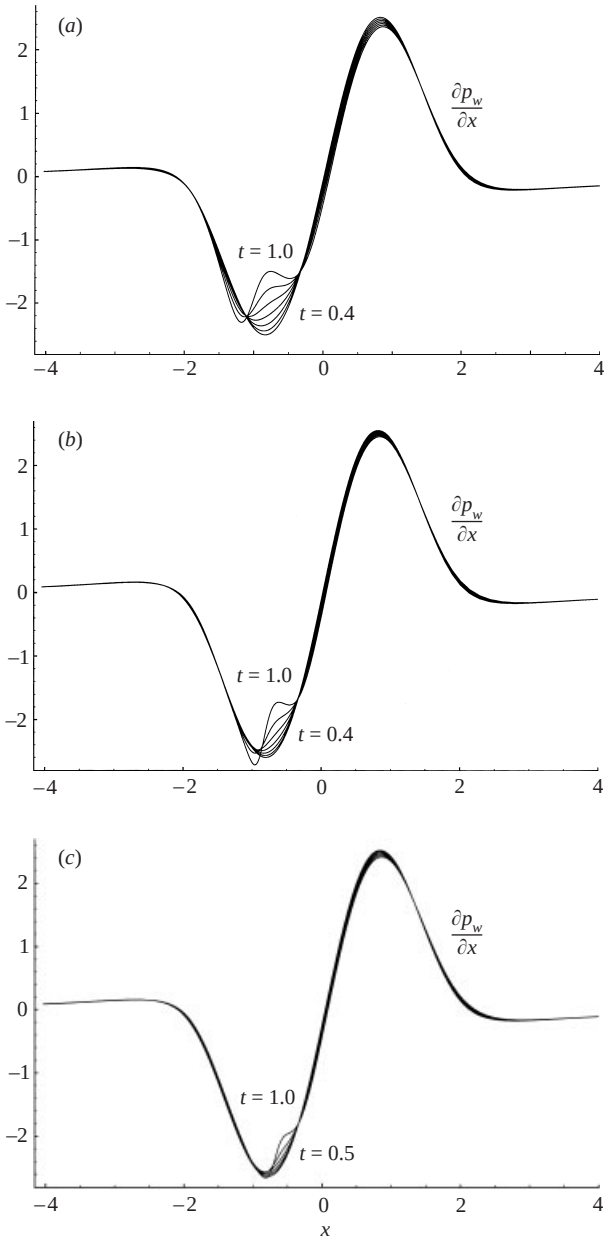

FIGURE 5. Streamwise pressure gradient along the surface in increments of $t = 0.1$ from Navier–Stokes solutions. (*a*) $Re = 10^3$, (*b*) $Re = 10^4$, (*c*) $Re = 10^5$.

thickness as the Reynolds number is decreased. The most visible differences between the cases with $Re = 10^5$ and $Re = 10^4$ as compared to the boundary-layer solution at times close to the singularity time $t_s = 1.402$ is the splitting of the recirculation region into a series of corotating eddies and the formation of secondary recirculation regions beneath the primary recirculation zone (these are visible in figures 10*a* and 12*a*). The case with $Re = 10^5$ also reveals the presence of a second spike immediately downstream, i.e. to the left, of the primary spike. As will be described later, these additional features can be traced to the influence of large-scale interaction.

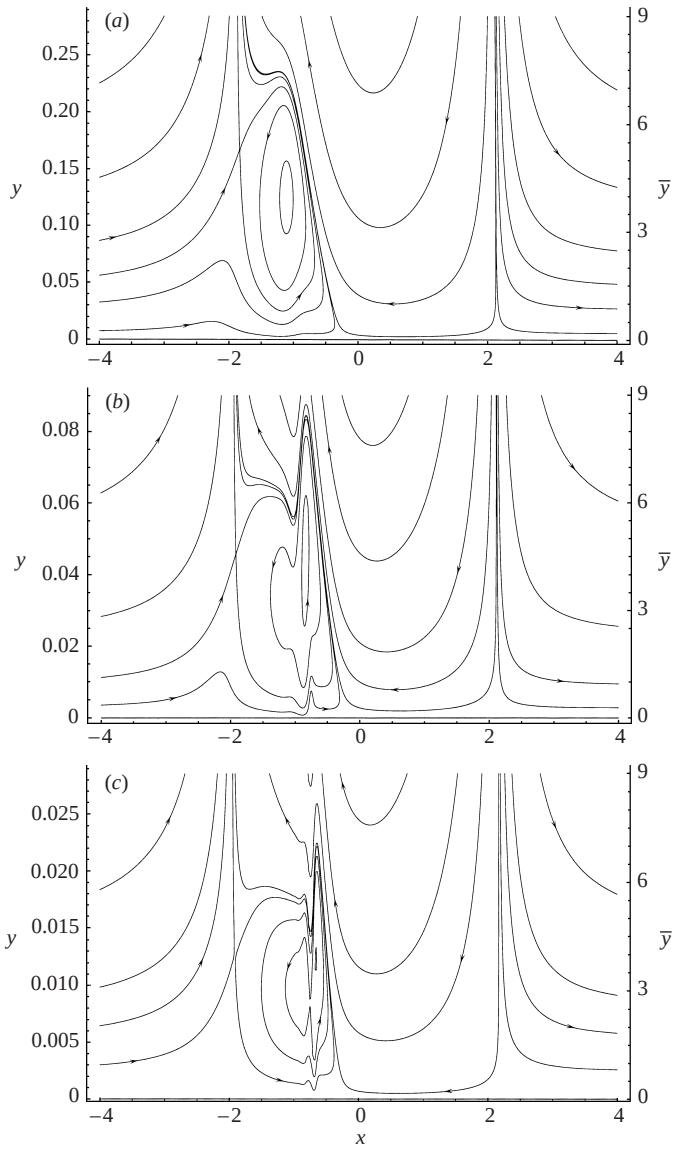

FIGURE 6. Streamlines from Navier–Stokes calculations. (*a*) $Re = 10^3$, $t = 1.4$, (*b*) $Re = 10^4$, $t = 1.4$, (*c*) $Re = 10^5$, $t = 1.3$.

Although the large-scale interaction begins later for higher Reynolds numbers, the spike formation occurs slightly earlier for $Re = 10^5$ than for $Re = 10^4$. In both cases, however, it is prior to the time t_{spike} at which the spike begins to form in the non-interacting boundary-layer results. This supports the conclusion of Peridier *et al.* (1991*b*) that interaction accelerates the unsteady separation process. This acceleration, however, had been attributed to what is here referred to as small-scale interaction which is induced by the spike. In order for the spike formation process itself to be accelerated, however, it must be due to the large-scale interaction that begins prior to formation of the spike. With hindsight, this appears to be consistent with the interacting boundary-layer results of Peridier *et al.* (1991*b*) in that interaction

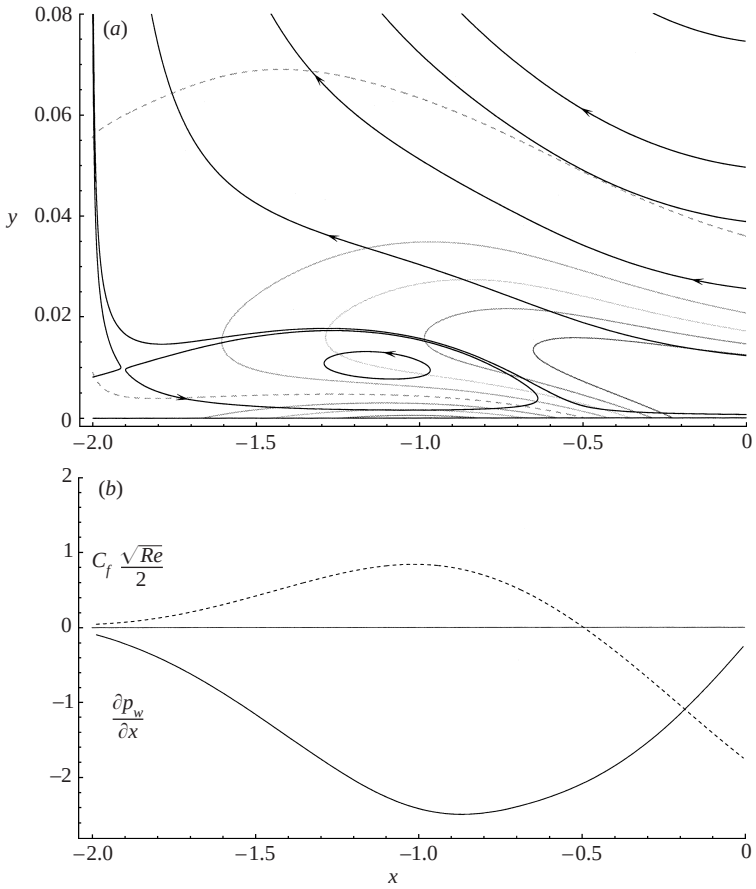

FIGURE 7. Results for $Re = 10^4$ at $t = 0.7$. (a) Streamlines and vorticity contours (minimum $\omega = -94\frac{2}{3}$; maximum $\omega = 94\frac{2}{3}$; increment $\omega = 23\frac{2}{3}$; dashed line is $\omega = 0$), (b) streamwise pressure gradient along the surface (solid) and skin friction coefficient (dashed).

must begin prior to formation of the spike because the interacting boundary-layer singularity time t_{sI} was not only prior to the non-interactive singularity time t_s, but in some cases was found to occur prior to the time t_{spike} at which the spike begins to form in the non-interactive calculation (cf. Peridier *et al.* 1991*a*). Therefore, the acceleration could not be caused, at least initially, by the small-scale interaction induced by the spike.

The results for $Re = 10^3$ at $t = 1.4$ shown in figure 6(a) are significantly different from those for the higher Reynolds numbers. There is no spike on the upstream side of the recirculation region (or if there is a spike, its streamwise width is comparable in size to the recirculation region), the recirculation region has not split, and no secondary recirculation regions exist at $t = 1.4$. As would be expected, owing to normal pressure gradients, or possibly streamwise diffusion, there is a Reynolds number below which the spike does not form at all on a scale distinct from that of the recirculation region; therefore, there is no subsequent small-scale interaction. For the thick-core vortex considered here, this critical Reynolds number is in the range $1 \times 10^3 < Re < 3 \times 10^3$.

These results, along with the high-Reynolds-number theory (see Doligalski *et al.* 1994, and the references therein), suggest that in terms of viscous–inviscid interaction

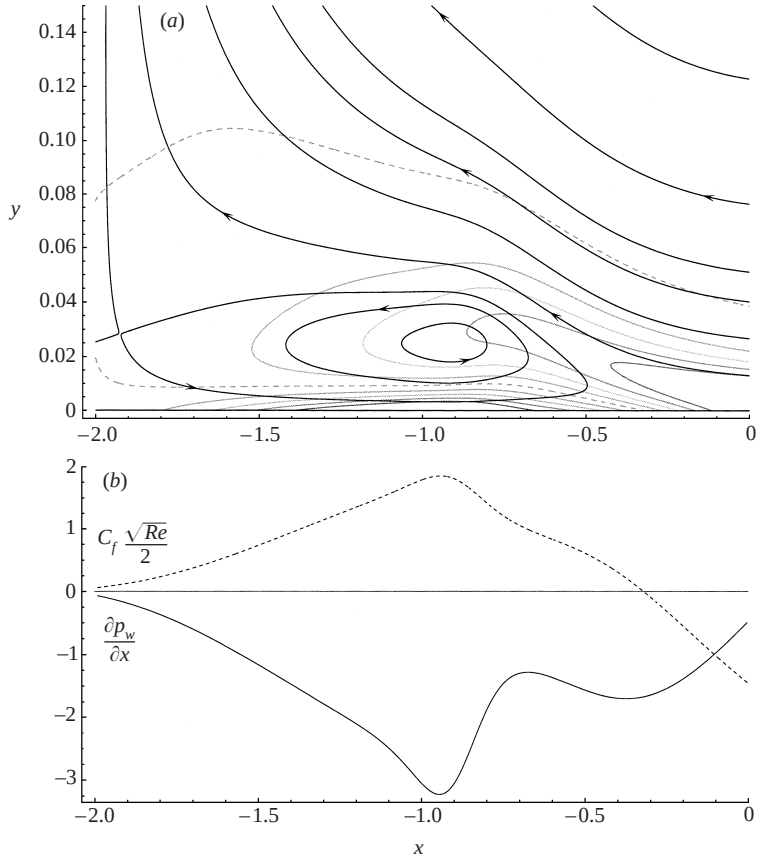

FIGURE 8. $Re = 10^4$ at $t = 1.1$. For caption details see figure 7.

there are three Reynolds-number regimes. In the low-Reynolds-number regime there is a large-scale interaction, apparently due to the developing strong outflows immediately upstream of the recirculation region, but no subsequent spike formation on a scale distinct from the large-scale interaction; therefore, there is no small-scale interaction. In the moderate-Reynolds-number regime, exemplified by the results for $Re = 10^4$ and 10^5, the large-scale interaction occurs as in the low-Reynolds-number regime followed by spike formation and small-scale interaction. In the high-Reynolds-number regime, either there is no large-scale interaction at all, as in the limiting case as $Re \to \infty$, or it begins too late to influence the flow evolution substantially; instead, there is only small-scale interaction provoked by the erupting spike. It has not been possible in this investigation to determine the critical Reynolds number between the moderate- and high-Reynolds-number regimes.

In order to illustrate the details of the flow development in the moderate-Reynolds-number regime and the mechanism by which large-scale interaction accelerates and modifies the unsteady separation process, a detailed series of results from a Navier–Stokes calculation are given for the case with $Re = 10^4$ in figures 7–11. Each figure shows the instantaneous streamlines superimposed on the vorticity contours in (a) and the streamwise pressure gradient along the surface and the skin friction coefficient in (b) for a series of times: $t = 0.7$, 1.1, 1.3, 1.45 and 1.55 in figures 7 to 11, respectively. In these figures the minimum contour is $\omega = -94\frac{2}{3}$, the maximum contour is $\omega = 94\frac{2}{3}$,

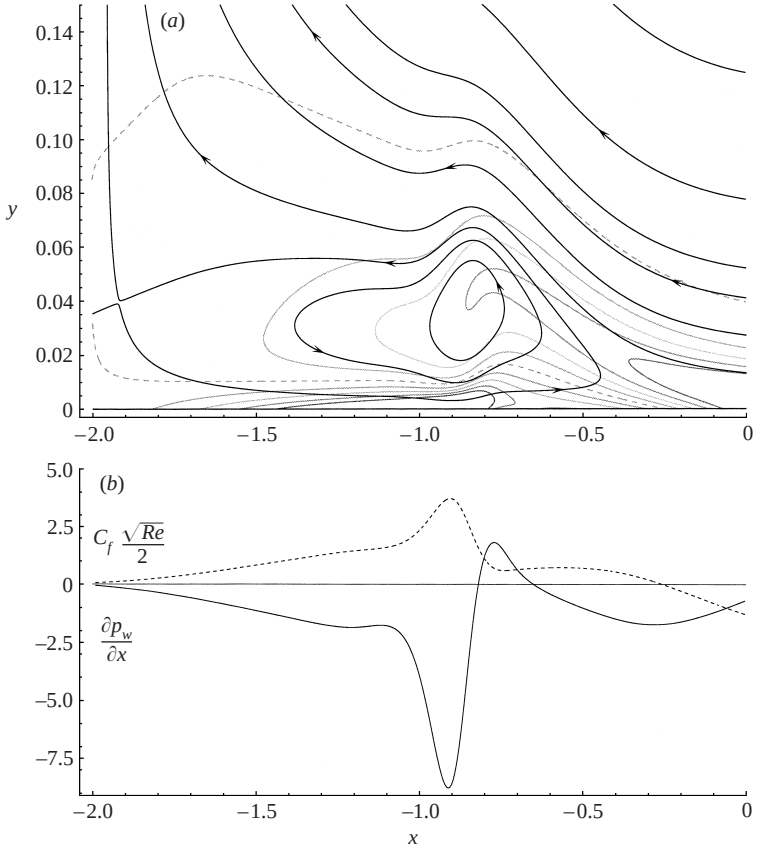

FIGURE 9. $Re = 10^4$ at $t = 1.3$. For caption details see figure 7.

and the $\omega = 0$ contour is dashed. The increment between each contour is $\omega = 23\frac{2}{3}$. The skin friction coefficient is determined from $C_f = -2Re^{-1}\omega_{|y=0}$. Note that the skin friction coefficient is scaled in the figures in order for it to be of the same order of magnitude as the streamwise pressure gradient with which it is plotted. Also note that the extent of the streamwise scale has been reduced in comparison to figure 6 in order to show the evolution of the flow within the boundary layer more clearly. In order to illustrate the near-wall flow evolution in the low-Reynolds-number regime, a similar sequence of results for $Re = 10^3$ is given in Obabko (2001).

Beginning at the impulsive start, positive vorticity is generated at the surface and is convected downstream in the negative x-direction. When the recirculation region forms at $t \approx 0.4$, in agreement with the boundary-layer results, negative vorticity begins to be generated immediately beneath it. The resulting zero-vorticity line associated with the recirculation region is a necessary precursor to the MRS criterion for unsteady separation. As shown in figure 7 at $t = 0.7$, the recirculation region has grown in size normal to the surface and is moving upstream against the oncoming flow in the bottom portion of the thick-core vortex. This is approximately the time at which large-scale interaction begins, leading to local changes in the streamwise pressure gradient. This change is clearly visible at $t = 1.1$ in figure 8(b) with the formation of a local maximum in the vicinity of $x = -0.7$. It is at this time that a small spike begins to form on the recirculation region at $x \approx -0.85$; this spike then grows rapidly in the direction normal

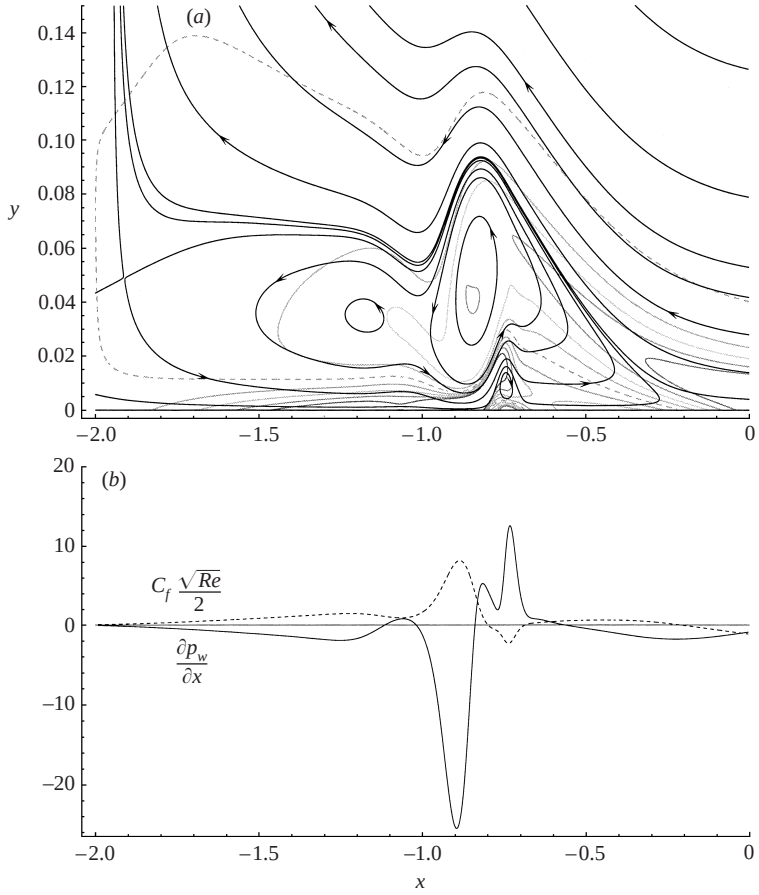

FIGURE 10. $Re = 10^4$ at $t = 1.45$. For caption details see figure 7.

to the surface as evidenced by the streamlines at subsequent times. At $t = 1.3$, the pressure gradient in the large-scale interaction region becomes positive (see figure 9*b*), i.e. locally adverse from the point of view of the flow beneath the recirculation region, leading to the formation of a secondary recirculation region that is evident near $x = -0.75$ at $t = 1.45$ as shown in figure 10(*a*). Observe that this secondary recirculation region causes the negative vorticity convecting in the positive x-direction near the wall to be lifted away from the surface and the primary recirculation region to be distorted from below. Also at this time, a small region of positive vorticity has begun to form at the surface, i.e. $C_f < 0$, beneath the secondary recirculation region.

Whereas the spike on the primary recirculation region does not begin to form until $t_{spike} \approx 1.3$ in the non-interacting boundary-layer results, the spike in the Navier–Stokes solutions for $Re = 10^4$ has already formed and grown substantially by this time. The mechanism by which large-scale interaction accelerates spike formation can be inferred from the evolution of the streamwise pressure gradient with time. At $t = 1.3$, the streamwise pressure gradient exhibits a minimum (figure 9*b*), i.e. locally favourable pressure gradient beneath the recirculation region, near $x = -0.9$ followed immediately by a local maximum near $x = -0.8$, which is an adverse pressure gradient with respect to the near-wall flow direction. This rapid increase in the streamwise pressure gradient in the near-wall flow direction causes the flow across the boundary

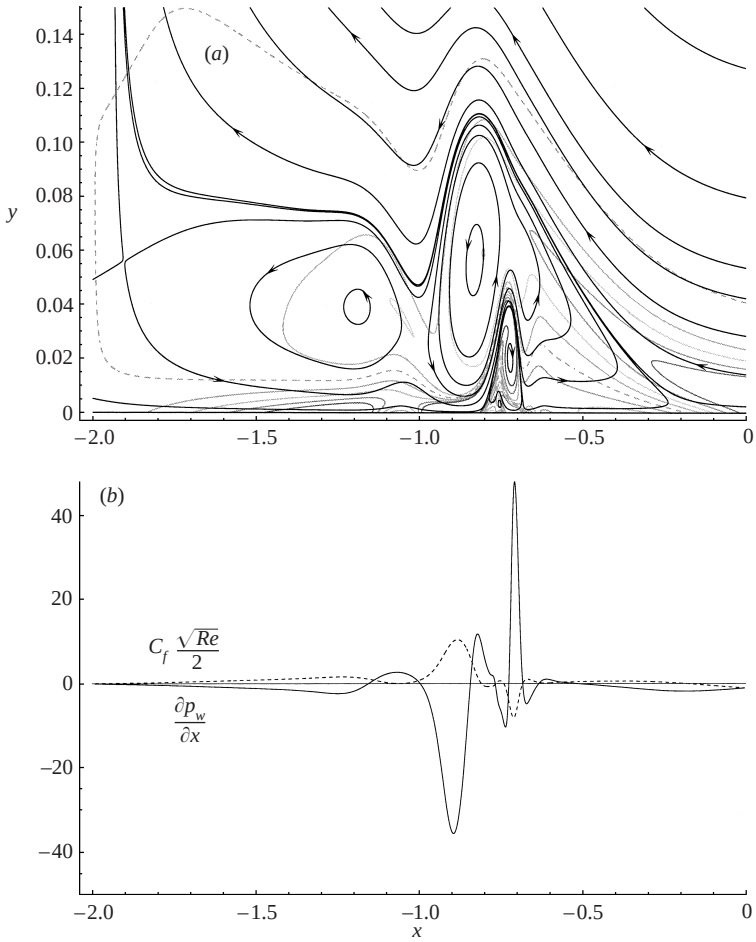

FIGURE 11. $Re = 10^4$ at $t = 1.55$. For caption details see figure 7.

layer to be compressed in the streamwise direction. This streamwise compression of a portion of the primary recirculation region leads to growth in the normal direction that accelerates formation of the spike in the region of rapid change in pressure gradient. It also induces an increase in skin friction at the same streamwise location as the minimum in pressure gradient (see, for example, figure 9). The magnitudes of these peaks in skin friction and streamwise pressure gradient increase rapidly with time and are indicative of the flow tending toward the interacting boundary-layer singularity in which these quantities become singular in the absence of normal pressure gradient effects (Smith 1988). The splitting of the recirculation region near $x = -1.0$ into two corotating eddies is also caused by changes in the streamwise pressure gradient. With respect to the near-wall flow direction, by $t = 1.3$ (figure 9) there is a rapid decrease in streamwise pressure gradient at this location causing the recirculation region to be stretched, eventually splitting by $t = 1.45$ (see figure 10).

These results show that it is the large-scale interaction and the changes it produces that are responsible for the accelerated spike formation, splitting of the primary recirculation region into corotating eddies, and formation of a secondary recirculation zone due to the locally adverse pressure gradient induced by the presence of the

primary recirculation region. Recall that all but the latter feature have been observed in at least some of the interacting boundary-layer results of Peridier *et al.* (1991*b*); without large-scale interaction these features do not occur (see Peridier *et al.* 1991*a*). Observe in figure 10 at $t = 1.45$ that the presence of the secondary recirculation region leads to the formation of a local minimum in streamwise pressure gradient at $x \approx -0.75$. This is analogous (but opposite in direction) to the local maximum in pressure gradient induced by the large-scale interaction that led to the formation of the secondary recirculation region. In the same way, the local minimum in pressure gradient caused by the secondary recirculation region becomes locally adverse, i.e. negative, near $x = -0.75$ at $t = 1.55$ (figure 11) and leads to formation of a tertiary recirculation region near $x = -0.75$. This cascade of eddies begetting smaller eddies is observed to occur over and over during the subsequent stages of the calculations in the moderate-Reynolds-number regime and is an important feature in determining the overall evolution of the flow field.

For comparison with the series of results described for $Re = 10^4$, the results for $Re = 10^5$ at $t = 1.35$ are shown in figure 12. As described previously, the large-scale interaction begins later as compared to $Re = 10^4$ and occurs over a shorter streamwise scale. The resulting changes in streamwise pressure gradient along the surface again cause the recirculation region to be compressed in the vicinity of $x = -0.65$, producing a spike, and stretched in the streamwise direction near $x = -0.7$, splitting the recirculation region into two corotating eddies. In addition to the shorter scales over which these events occur, the results for $Re = 10^5$ also reveal the formation of a secondary spike to the left of the primary spike. Just as for the primary spike, it is formed because of a streamwise compression as evidenced by the rapid increase in pressure gradient in the near-wall flow direction in the vicinity of $x = -0.825$ (see figure 12*b*).

In order to compare the Navier–Stokes solutions obtained here with the theory describing how normal pressure gradients modify the unsteady separation process (Hoyle *et al.* 1991; Li *et al.* 1998), results are given in figure 13 for the normal pressure gradient superimposed on streamwise velocity profiles at a series of streamwise locations for $Re = 10^5$ at $t = 1.35$, corresponding to figure 12. On the boundary-layer scale, the contours of normal pressure gradient are $\partial p/\partial \bar{y} = -0.1$, -0.03, -0.01, -0.001, 0.001, 0.01, 0.03, 0.1 and 0.3; on the physical scale, these contour levels correspond to $\partial p/\partial y = -31.6$, -9.5, -3.2, -0.3, 0.3, 3.2, 9.5, 31.6 and 94.9, respectively. The distance between the streamwise velocity profile stations where $u = 0$ corresponds to the magnitude of streamwise velocity equal to 3.0, which is comparable with the magnitude of the maximum inviscid velocity, $|U_e|_{max} \approx 2.5$, induced by the thick-core vortex. The dotted line is the normal location of the inflection points that occur in the streamwise velocity profile, and the dashed line is the zero-vorticity contour. Recall from the MRS criterion for unsteady separation that the non-interactive boundary-layer singularity, i.e. the terminal boundary-layer solution, occurs along the zero-vorticity line, and the vortex wind-up postulated by Hoyle *et al.* (1991) and Li *et al.* (1998) occurs in a critical layer surrounding the inflection point.

The normal pressure gradient remains negligible throughout the early stages of the calculation. Cassel (2000) determined that for $Re = 10^5$, normal pressure gradients begin to become an $O(1)$ influence on the flow (on the boundary-layer scale) at approximately $t = 1.2$. For example, the contour corresponding to $\partial p/\partial \bar{y} = 0.01$ ($\partial p/\partial y = 3.2$) does not appear until approximately $t = 1.25$. It then increases rapidly in magnitude such that by $t = 1.35$, the normal pressure gradient is of comparable magnitude to the streamwise pressure gradient (cf. figure 12*b*). A local maximum

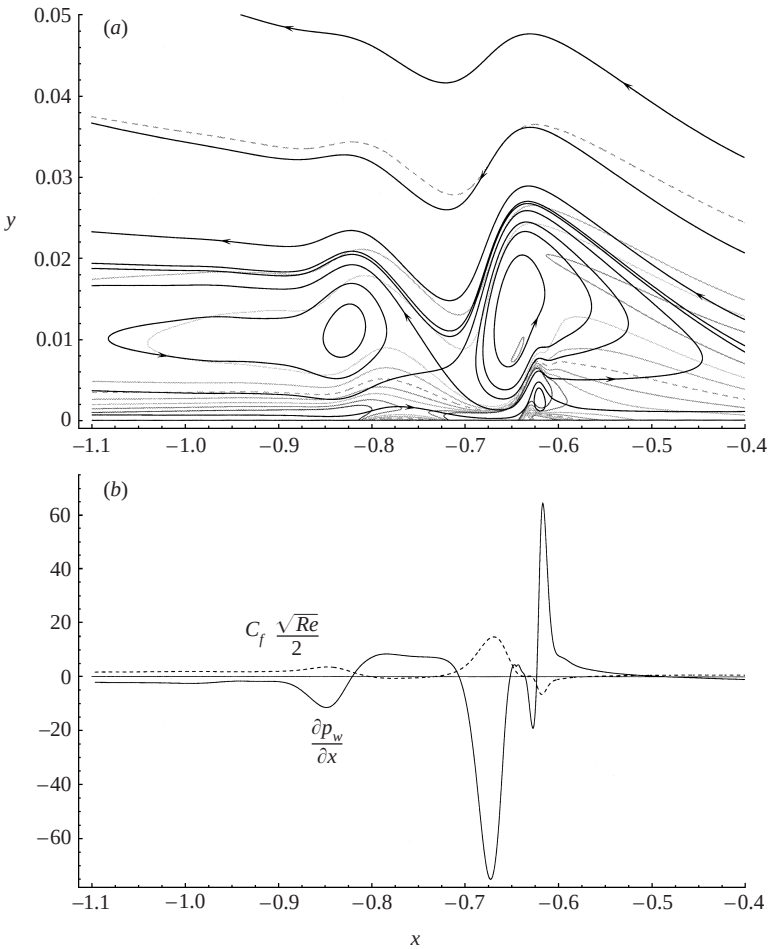

FIGURE 12. Results for $Re = 10^5$ at $t = 1.35$. (*a*) Streamlines and vorticity contours (dashed line is $\omega = 0$), (*b*) streamwise pressure gradient along the surface (solid) and skin friction coefficient (dashed).

begins to form immediately above the growing spike, which is after the time at which the spike begins to form and before the approximate time at which the interacting boundary-layer singularity would occur (see Cassel 2000), consistent with the theoretical sequence. At $t = 1.35$ this maximum is centred at approximately (−0.65, 0.025) in figure 13. A corresponding minimum forms near the wall at the same streamwise location and centred at approximately (−0.65, 0.004). This maximum and minimum pair is a consequence of the streamwise compression that occurs in this same location owing to the rapid increase in streamwise pressure gradient in the near-wall flow direction (see figure 12*b*). As the recirculation region is compressed in the streamwise direction, the flows above and below it are compressed in the normal direction causing an increase in the magnitude of the normal pressure gradient and a dampening of the growth of the spike in the direction normal to the wall. Note that the maximum and minimum pairs tend to form above and below the normal position of the inflection point in the streamwise velocity profiles as can be seen by the pair that is in an early stage of development near $x \approx -0.825$, where the secondary spike is forming. The

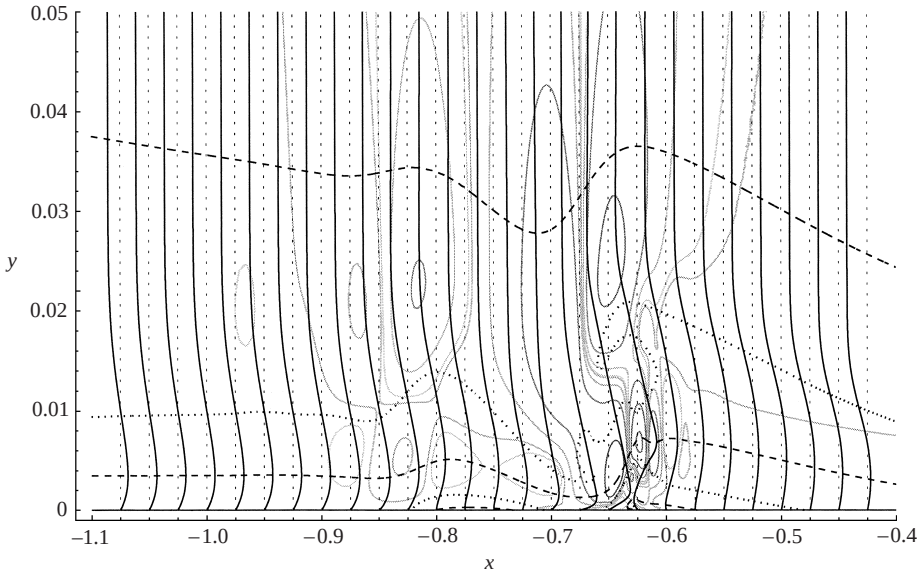

FIGURE 13. Normal pressure gradient contours and streamwise velocity profiles for $Re = 10^5$ at $t = 1.35$ (dashed line is $\omega = 0$ and dotted line is normal location of inflection points in streamwise velocity).

maximum in normal pressure gradient centred near (−0.625, 0.006) is a consequence of the growth, owing to a streamwise compression, of the secondary recirculation region that is forming near this same streamwise location (see figure 12). Although it is clear that the normal pressure gradient has become significant in the Navier–Stokes calculations, it is difficult to determine whether it does so in a manner consistent with the results of Li *et al.* (1998).

In order to gain greater insight into the differences between the low- and moderate-Reynolds-number regimes, namely the appearance or lack of a spike, the location of the rapid increase in streamwise pressure gradient in the near-wall flow direction that leads to accelerated spike formation is tracked with time for various Reynolds numbers in figure 14. More specifically, the streamwise location of the maximum slope in streamwise pressure gradient in this region is followed with time; movement in the positive x-direction is upstream with respect to the flow in the lower portion of the thick-core vortex. For comparison, the streamwise location of the non-interacting boundary-layer singularity is $x_s = -0.375$ (Cassel 2000). Beginning at approximately $t = 1.0$, when a well-defined maximum has developed, the compression region initially moves downstream for all cases except $Re = 10^5$. Whereas this trend continues for the case with $Re = 10^3$, the other cases have a period of time during which there is an upstream movement of the compression region. For example, this occurs for $1.2 < t < 1.5$ for the case with $Re = 3 \times 10^4$. This upstream movement is more pronounced as the Reynolds number is increased. The upstream movement of the compression region is eventually reversed owing to generation and growth of a region of negative near-wall vorticity (see, for example, figure 11*a*) that weakens the near-wall structure allowing it to convect downstream.

3.2. *Post-eruptive behaviour*

In the previous section, results of the Navier–Stokes calculations have been described for the unsteady separation induced by a thick-core vortex through the early stages of

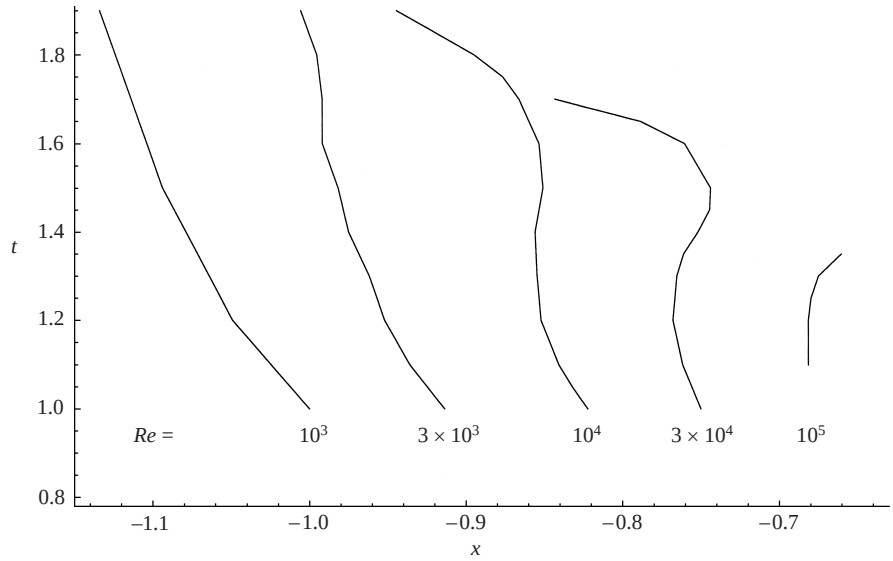

FIGURE 14. Location of maximum slope in streamwise pressure gradient in the spike formation region for various Reynolds numbers.

development including large-scale interaction, spike formation and subsequent small-scale interaction and normal pressure gradient effects. This corresponds to the stages for which the theory for unsteady separation has been developed and roughly up to the time at which the non-interactive boundary-layer singularity occurs, i.e. $t_s = 1.402$. For some of the cases considered, it was possible to continue the calculations well beyond this time and observe the mechanisms by which the unsteady separation process leads to a pulling away of the primary recirculation region and detachment of the thick-core vortex; these results are described here.

Returning to the case with $Re = 10^4$, a series of results are shown in figures 15 and 16. Note that the extent of the horizontal scale has been reduced and that of the vertical scale has been expanded in figure 15 as compared to that in figure 11. Figure 15(a) shows the instantaneous streamlines and vorticity contours at time $t = 1.9$. By this time the negative vorticity associated with the secondary recirculation region observed at $t = 1.55$ (see figure 11a) is ejected, splitting the primary recirculation region near $x = -0.8$ to form what Brinckman & Walker (2001) refer to as an 'alleyway' in the streamlines and a 'spike-like finger' in the vorticity field. The primary recirculation region produced by the adverse pressure gradient, which is induced by the thick-core vortex, has by this time split into three eddies; the one centred near $x \approx -0.95$ originated as the spike, the eddy centred near $x = -1.25$ split at $t \approx 1.4$ owing to a streamwise expansion, and the eddy near $x = -0.7$ was split off owing to the ejection of near-wall vorticity near $x = -0.8$. As shown in figure 15(b) at $t = 2.3$, the eddy that was centred at approximately $x = -1.2$ at $t = 1.55$ and $x = -1.25$ at $t = 1.9$ merges with the larger eddy upstream as the vorticity contained within the downstream eddy winds around the upstream eddy. In addition, another eddy near $x = -0.5$ has split off the original primary recirculation region owing to the normal growth of the secondary eddy that was centred near $x = -0.55$ at $t = 1.9$. The flow structure observed at $t = 1.9$ and $t = 2.3$ is representative of the results for Reynolds numbers within the moderate-Reynolds-number regime with the splitting of the primary recirculation region into a series of corotating eddies, formation

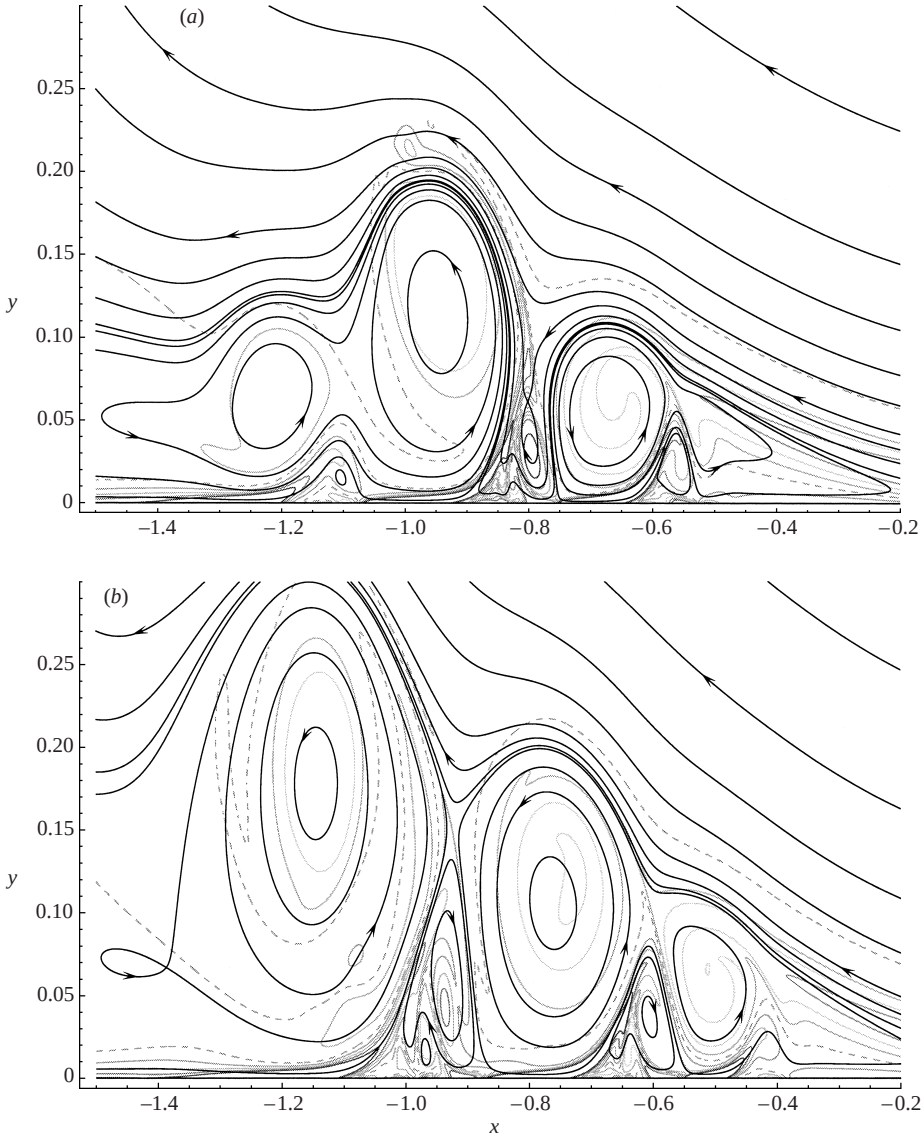

FIGURE 15. Instantaneous streamlines and vorticity contours for $Re = 10^4$ (dashed line is $\omega = 0$). (a) $t = 1.9$, (b) $t = 2.3$.

of corresponding secondary recirculation regions, and multiple ejections of near-wall vorticity. These features are also evident in the results of Brinckman & Walker (2001).

In order to observe the interaction between the growing eddies and the thick-core vortex on the scale of the vortex, the extent of the horizontal and vertical scales have been expanded in figure 16. The three eddies observed at $t = 2.3$ in figure 15(b) are visible on the scale of the thick-core vortex in figure 16(a), which shows the instantaneous streamlines and vorticity contours at $t = 2.5$. By $t = 3.0$, the two largest of these eddies have merged, as shown in figure 16(b), in a manner similar to that observed between $t = 1.9$ and $t = 2.3$ (see figure 15). This amalgamated eddy is then observed to pull away from the surface in what is probably a predominantly inviscid

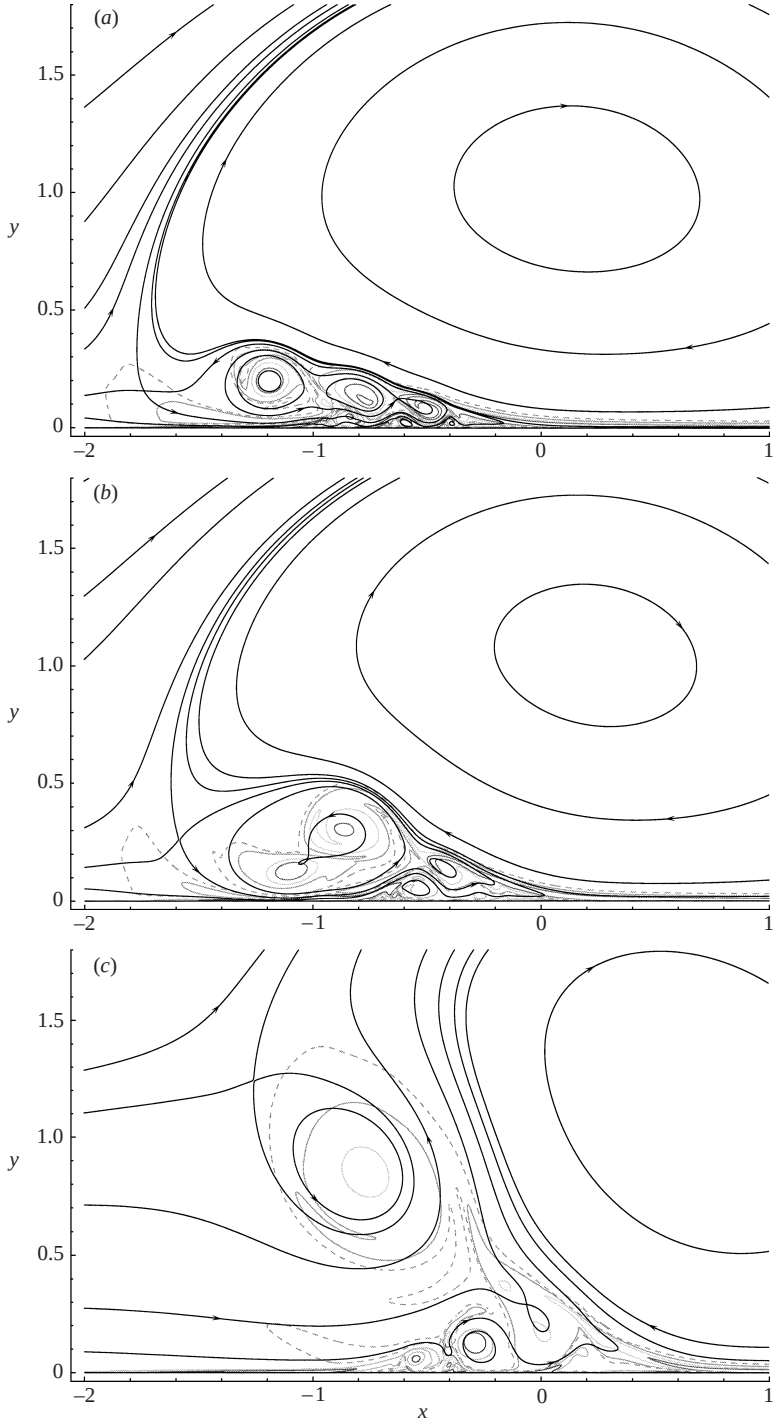

FIGURE 16. Instantaneous streamlines and vorticity contours for $Re = 10^4$ (dashed line is $\omega = 0$). (*a*) $t = 2.5$, (*b*) $t = 3.0$, (*c*) $t = 4.5$.

interaction between this portion of what was once the primary recirculation region and the thick-core vortex. As shown in figure 16(*c*), this process leads to 'detachment' of the vortex, which up until this time has not moved substantially from its inviscid location $(x_c, y_c) = (0, 1)$, and convection downstream with the freestream flow. Vortex detachment, therefore, appears to be a process involving the weakening of the thick-core vortex owing to interaction with opposite sign vorticity originally introduced into the flow by the unsteady boundary-layer separation process. Note that at $t = 4.5$ (figure 16*c*), the secondary structures exhibit similar behaviour to that observed in the primary recirculation region at earlier times, for example, splitting of the secondary eddy and ejection of near-wall vorticity near $x = -0.4$. It has been shown in a companion study (Obabko 2001; Obabko & Cassel 2002) that the detachment process for $Re = 10^3$, which is representative of the low-Reynolds-number regime, is remarkably similar to that in the moderate-Reynolds-number regime despite the very different near-wall flow evolution.

For comparison with these results for $Re = 10^4$, results are shown for another Reynolds number within the moderate-Reynolds-number regime, $Re = 3 \times 10^4$, at $t = 1.7$ in figure 17(*a*). As for $Re = 10^4$, the primary recirculation region is split into a series of eddies by streamwise expansion near $x = -0.95$ and successive ejections of negative near-wall vorticity near $x = -0.75$, $x = -0.6$ and $x = -0.5$, in turn. Immediately upstream of the eddies centred near $x = -1.1$ and $x = -0.85$, the near-wall vorticity is ejected abruptly away from the surface and wraps around the respective eddies. At subsequent times, the downstream eddies begin to merge prior to their movement away from the surface and subsequent vortex detachment (not shown), just as for the case with $Re = 10^4$. More detailed results for the case with $Re = 3 \times 10^4$ are given in Obabko (2001).

Finally, we comment on the instability observed in the Navier–Stokes calculations of Brinckman & Walker (2001) for a similar vortex-induced flow. High-frequency oscillations in vorticity were observed to occur in regions between eddies, referred to as alleyways, where the streamlines sweep down toward the surface then back out again. These oscillations were attributed to the possible presence of a Rayleigh instability that can occur once there is an inflection point in the velocity profile. Similar oscillations have been observed in the present calculations under certain conditions. For example, figure 17(*b*) shows the zero-vorticity line for a calculation with $Re = 3 \times 10^4$ at $t = 1.7$. This is at the time shown in figure 17(*a*) but from a calculation carried out on a grid with a quarter the resolution in the streamwise direction (1025×513) and a larger time step ($\Delta t = 3 \times 10^{-6}$ compared to $\Delta t = 2 \times 10^{-6}$). Just as in Brinckman & Walker (2001), the subsequent ejection of near-wall vorticity in the regions between eddies (near $x = -1.0$ and $x = -0.75$) is followed by the development of high-frequency oscillations in vorticity. The increased spatial and temporal resolution used in the calculation shown in figure 17(*a*), however, substantially delays the onset of the instability. For some of the Reynolds numbers considered, the oscillations have been completely removed by increasing the resolution, and the calculations have been carried out through to vortex detachment. For the case with $Re = 10^4$, for example, a grid with 513×513 points produces oscillations similar to those observed in figure 17(*b*). On a 1025×513 grid, minor inaccuracies begin to appear at approximately $t = 1.75$ near saddle points in the vorticity field in the vicinity of the region between the central and right eddies. Small oscillations then begin to appear and grow until approximately $t = 1.85$ after which the oscillations disappear, roughly coinciding with the time at which local ejection of vorticity occurs in this region. Note that these oscillations are not visible on the scale shown in

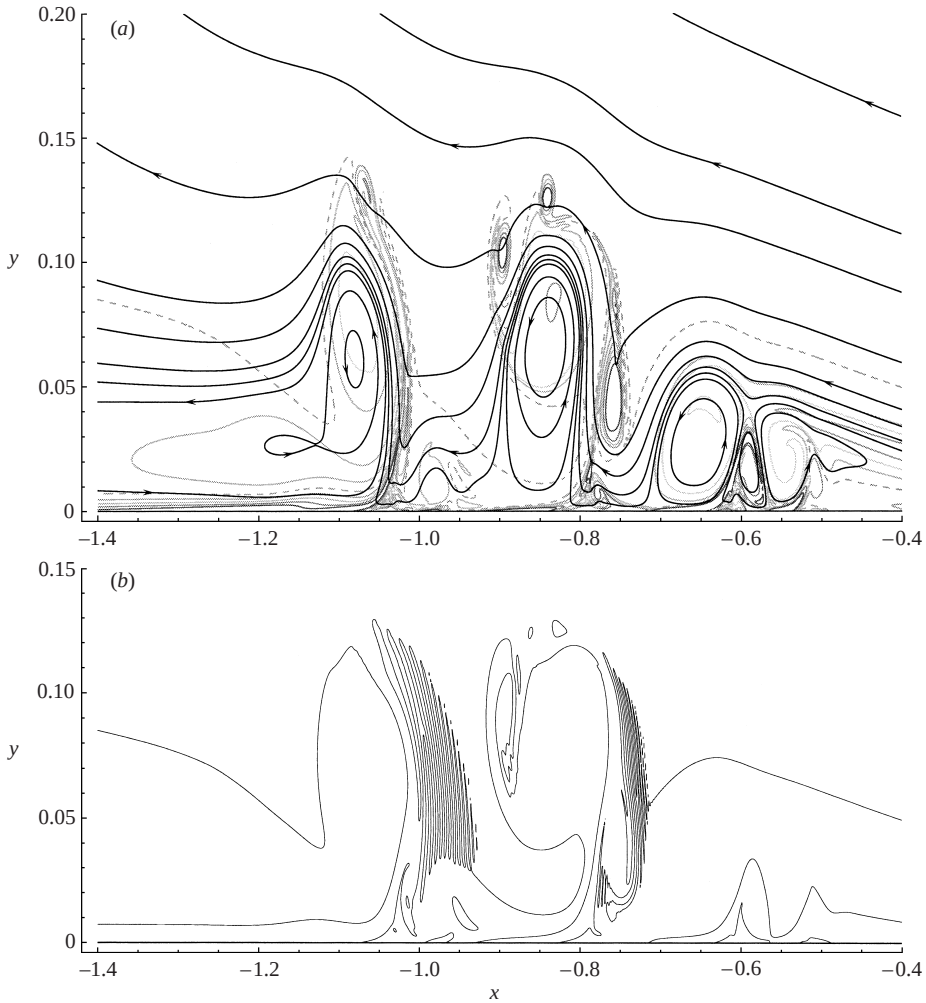

FIGURE 17. Results for $Re = 3 \times 10^4$ at $t = 1.7$. (*a*) Streamlines and vorticity contours (dashed line is $\omega = 0$), (*b*) zero-vorticity contour for case with instability.

figure 15(*a*). On a grid with 2049×513 points, the inaccuracies in vorticity are even less pronounced and do not lead to any oscillations. It appears that the initial growth of the instability is greatly affected by the spatial resolution, such that the perturbations due to increased inaccuracies on the coarser grids are amplified by the instability leading to high-frequency oscillations.

4. Discussion

Solutions of the unsteady Navier–Stokes equations have been obtained for the flow induced by a thick-core vortex convecting above a surface in a uniform flow. These results show that in terms of the nature of interaction between the viscous boundary layer and the inviscid outer flow, the unsteady separation process evolves differently in three Reynolds-number regimes, as shown schematically in figure 18 (cf. figure 1). The times shown in the figure are approximate values at which each of the stages begins in the non-interacting boundary-layer solution (figure 18*a*) and the Navier–

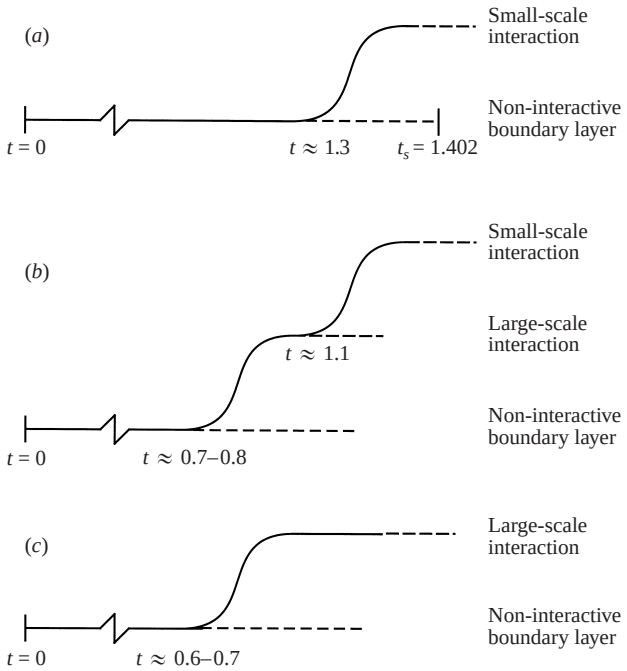

FIGURE 18. Schematic of the three Reynolds-number regimes for viscous–inviscid interaction in unsteady separation. (*a*) High-Reynolds-number regime, e.g. $Re \to \infty$, (*b*) moderate-Reynolds-number regime, e.g. $Re = 10^4$, (*c*) low-Reynolds-number regime, e.g. $Re = 10^3$.

Stokes solutions at the Reynolds numbers listed in the captions for figures 18(*b*) and 18(*c*). At high Reynolds numbers (e.g. $Re \to \infty$), exemplified by solutions of the non-interactive boundary-layer equations, the flow begins to develop a very sharp spike at $t_{spike} \approx 1.3$ that evolves toward a singularity at $t_s = 1.402$. Just prior to formation of the boundary-layer singularity, the growing spike provokes a small-scale interaction with the outer inviscid flow requiring another reduced set of equations. This is represented by the second tier in figure 18(*a*). This small-scale interaction was thought to be governed by the so-called first interactive stage formulated by Elliott *et al.* (1983) and solved numerically by Cassel *et al.* (1996). At moderate Reynolds numbers (e.g. $Re = 10^4$), the flow develops initially in the same manner as in the high-Reynolds-number case; however, a large-scale interaction begins well before the formation of the spike (the second tier in figure 18*b*). One consequence of the large-scale interaction in the moderate-Reynolds-number regime is an acceleration of the process that leads to spike formation; the spike then provokes a small-scale interaction (the third tier in figure 18*b*). At low Reynolds numbers (e.g. $Re = 10^3$), large-scale interaction begins just as in the moderate-Reynolds-number case; however, no spike forms at later times on a streamwise scale that is distinct from that of the primary recirculation region, thus eliminating the small-scale interaction as depicted in figure 18(*c*).

It appears that it is the development of a locally strong outflow within the boundary layer that initiates the large-scale interaction, whereas it is the formation of a sharp, rapidly growing spike that initiates the small-scale interaction. This outflow begins to develop immediately upstream (to the right) of the primary recirculation region which acts as a barrier and causes the flow to change directions abruptly in order

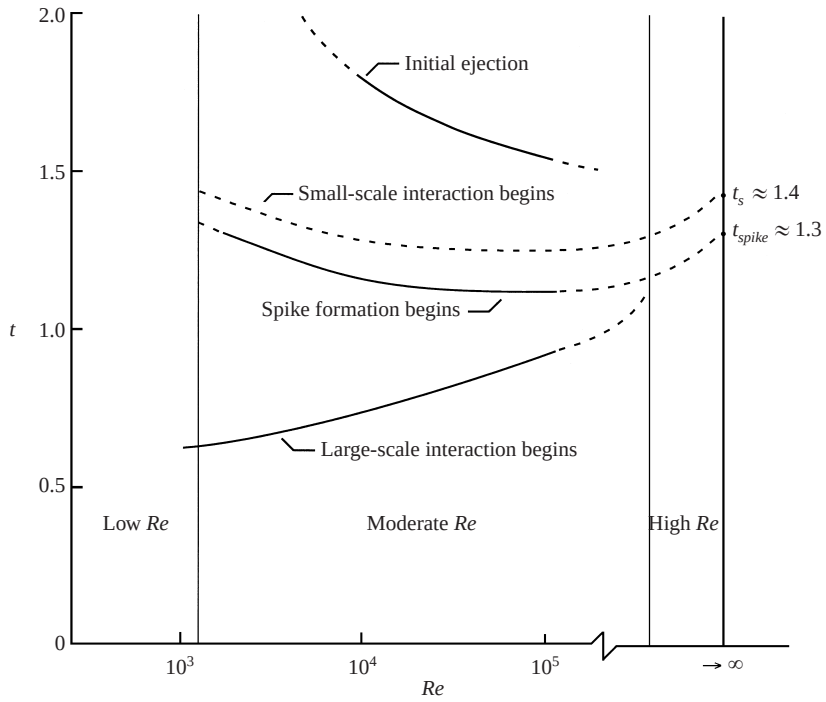

FIGURE 19. The times at which significant events occur within the three Reynolds-number regimes.

to pass over it. Solutions in the moderate-Reynolds-number regime are marked by a distinct upstream movement of the primary recirculation region that intensifies this outflow and contributes to spike formation.

An alternative depiction of the Reynolds-number regimes is shown in figure 19, where the times at which the large-scale interaction, spike formation, small-scale interaction and initial vorticity ejection begin are shown schematically. Note that solid lines represent estimated times from the Navier–Stokes calculations of the thick-core vortex, dashed lines represent conjecture, and the times t_s and t_{spike} are from a boundary-layer calculation of the thick-core vortex (Cassel 2000). The ejection time t_e is taken as the moment when negative vorticity penetrates through the primary recirculation region. Because the thickness of the boundary layer is $O(Re^{-1/2})$, the effect of the large-scale interaction diminishes, becoming important later in the solution, as the Reynolds number increases, and ultimately vanishing as $Re \rightarrow \infty$. In contrast, over the range of Reynolds numbers considered, the spike begins to form and the subsequent small-scale interaction begins earlier in time with increasing Reynolds number. This is due to the increased compressive effect across the boundary layer in the streamwise direction as Reynolds number is increased. The time at which the spike begins to form, however, must then increase to match the limiting-Reynolds-number case, i.e. $t_{spike} \approx 1.3$, suggesting that there is a critical Reynolds number at which it is a minimum. This is probably due to two competing influences. At lower Reynolds numbers, the large-scale interaction begins earlier, but the resulting streamwise compression occurs over a larger streamwise scale and evolves more slowly. At higher Reynolds numbers, on the other hand, the large-scale interaction begins later but leads to a more rapid compression and subsequent spike formation.

In the moderate-Reynolds-number regime, the upstream motion of the compression region diminishes, the streamwise width of the spike increases and its growth rate slows as the Reynolds number decreases, until the low-Reynolds-number regime is reached, below which no spike forms and there is no small-scale interaction. It has not been possible with the calculations presented here to determine the upper limit of the moderate-Reynolds-number regime, above which no large-scale interaction occurs. It is possible that the large-scale interaction is an important feature in unsteady separation for all but the limit as $Re \to \infty$ and must be accounted for in the high-Reynolds-number asymptotic theory. This may be the cause of the immediate breakdown of the first interactive stage (see Cassel *et al.* 1996), which only accounts for the small-scale interaction associated with the growing spike.

It should be emphasized that the large-scale interaction that occurs in the moderate-Reynolds-number regime is not simply a finite-Reynolds-number modification of the boundary-layer results, for example a spike with finite thickness rather than zero thickness as $Re \to \infty$, but rather it leads to a different sequence of physical events that significantly alters the flow for moderate Reynolds numbers. The additional features that appear in the solutions for cases within the moderate-Reynolds-number regime, but not the high-Reynolds-number regime, can all be traced to the influence of the large-scale interaction. This large-scale interaction begins to have a significant influence on the flow development well before spike formation begins in the non-interacting boundary-layer results. It leads to changes in the streamwise pressure gradient within the boundary layer that evolve into a region of streamwise compression of a portion of the recirculation region owing to a rapid increase in the pressure gradient in the near-wall flow direction. This streamwise compression contributes to the growth that occurs in the direction normal to the surface resulting in an acceleration of spike formation. In addition, regions of local expansion occur in the streamwise direction, where the pressure gradient decreases rapidly in the near-wall flow direction, causing the recirculation region to split into multiple corotating eddies. The locally adverse pressure gradients due to each of these eddies then lead to formation of a series of secondary recirculation regions. The growth of the secondary recirculation regions also leads to splitting of the primary eddies as near-wall vorticity is ejected away from the surface. Several of these features have also been observed in the Navier–Stokes solutions obtained by Brinckman & Walker (2001) for a similar vortex-induced flow. It is interesting to note that the duration in time from the impulsive start to the time at which the non-interacting boundary-layer singularity occurs, $t_s = 1.402$, roughly corresponds to a one-third turn of the thick-core vortex, illustrating how rapidly the unsteady separation process is initiated and evolves toward a significant eruption.

After interaction becomes important, normal pressure gradients, which are zero to leading order in the non-interacting boundary-layer equations, become large locally in order to avoid the interacting boundary-layer singularity (Smith 1988). Li *et al.* (1998) predict that the presence of normal pressure gradients and an associated critical layer containing the inflection point in the streamwise velocity profiles leads to a 'vortex wind-up.' Although the formation of multiple eddies in the Navier–Stokes solutions obtained here bears some resemblance to this vortex wind-up, the process observed here appears to have as much to do with the evolution of the streamwise pressure gradient, which results from the interaction, as it does with normal pressure gradient effects (at least at the Reynolds numbers considered here). It may be that the presence of normal pressure gradients simply retards the growth of the spike in the normal direction, thus preventing the interacting boundary-layer singularity, and allowing time for the natural tendency of separated vorticity layers to roll up and form

discrete vortices. Alternatively, it is possible that the cause and effect relationships involving streamwise pressure gradients observed in this investigation are unified with the normal pressure gradient effects (including vortex wind-up) by the theory of Li *et al.* (1998).

Results for two cases in the moderate-Reynolds-number regime, $Re = 10^4$ and $Re = 3 \times 10^4$, have also been shown for times well past that at which interaction and spike formation first begin. These results reveal a process in which the primary recirculation region interacts with the surface and produces a cascade of secondary and tertiary eddies, each of which forms successively upstream (in a local sense) from the previous one. Each secondary eddy then grows, splitting the primary recirculation region and ejecting near-wall vorticity into the outer flow. As the Reynolds number increases, the time of the initial ejection t_e is found to tend toward the time of the erupting singularity of Cassel (2000) in the limit $Re \to \infty$ (see figure 19). A similar trend is observed for the streamwise location of the vorticity ejection x_e.

While the process of splitting the primary recirculation region into a series of corotating eddies repeats itself on the upstream side of the separation structure, the eddies that originated from the primary recirculation region then begin to merge sequentially from the downstream side of the structure. Ultimately, the largest of the merged eddies, which contains vorticity having opposite sign as compared to the thick-core vortex, moves away from the surface and interacts with the vortex, causing it to detach and convect downstream with the freestream velocity. This unsteady separation process is very similar to that observed in flow visualizations of juncture flows in which a series of eddies form within the boundary layer upstream of an obstacle leading to several ejections of near-wall vorticity in thin spires and a subsequent merging of the eddies (see, for example, Seal *et al.* 1995, 1997). Also note that the splitting of eddies and formation of secondary eddies have been detected experimentally by Bouard & Coutanceau (1980). The merging of eddies and vorticity ejections that contribute to splitting of the primary recirculation region may be observed also in numerical solutions of the two-dimensional incompressible flow around a circular cylinder (Koumoutsakos & Leonard 1995).

Although the near-wall flow development is very different in the low- and moderate-Reynolds-number regimes, the detachment process is observed to be very similar. Therefore, the fact that the spike forms and vorticity ejection occurs in the moderate-Reynolds-number regime, but not in the low-Reynolds-number regime, appears to play a secondary role in terms of the vortex detachment process. In fact, for cases in the low-Reynolds-number regime, such as $Re = 10^3$, detachment occurs earlier in non-dimensional time than for cases within the moderate-Reynolds-number regime, such as $Re = 10^4$ (Obabko 2001; Obabko & Cassel 2002). Although spike formation and vorticity ejection are two of the critical features in the near-wall flow development, they do not appear to be good indicators of whether the vortex will detach, at least not for the range of Reynolds numbers considered in this investigation. It is possible that this may change as the Reynolds number is increased and the eruption intensifies.

A similar vortex-induced problem was considered by Brinckman & Walker (2001) who have observed the development of a high-frequency oscillation in vorticity in regions, referred to as alleyways, where the streamlines from the outer flow sweep down toward the wall. A similar instability was observed to occur in some of the cases in the present investigation; however, it was possible to delay and sometimes remove the oscillations by increasing the spatial and temporal resolution. The fact that calculations of two similar flows using different algorithms both produce very similar oscillations suggests that the instability is not purely numerical, but

apparently has some physical basis. This is supported by the results of Brinckman & Walker (2001) who found that the approximate wavenumber of the instability has a Reynolds-number scaling that is consistent with a Rayleigh instability. The somewhat different behaviour of the instability in the two sets of calculations is probably due to differences in spatial and temporal resolution and/or problem dependencies. For example, Brinckman & Walker consider a model problem in which the external flow that induces the evolution of the near-wall flow is uncoupled from the developing viscous response, whereas in this investigation the entire flow field, including the thick-core vortex, is computed. From the results of this investigation, it appears that refining the grid reduces inaccuracies that develop in the vicinity of saddle points in the vorticity field. It is possible that it is these inaccuracies that provide the initial perturbation that then grows according to the instability observed by Brinckman & Walker (2001).

This work was supported by the US Army Research Office under grant number DAAG55-98-1-0384, Dr Thomas L. Doligalski, technical monitor. The authors would like to thank R. I. Bowles, F. T. Smith and J. D. A. Walker for valuable discussions regarding this work.

REFERENCES

Batchelor, G. K. 1967 *An Introduction to Fluid Dynamics*. Cambridge University Press.

Bouard, R. & Coutanceau, M. 1980 The early stages of development of the wake behind an impulsively started cylinder for $40 < Re < 10^4$. *J. Fluid Mech.* **101**, 583–607.

Brinckman, K. W. & Walker, J. D. A. 2001 Instability in a viscous flow driven by streamwise vortices. *J. Fluid Mech.* **432**, 127–166.

Cassel, K. W. 2000 A comparison of Navier–Stokes solutions with the theoretical description of unsteady separation. *Phil. Trans. R. Soc. Lond.* A **358**, 3207–3227.

Cassel, K. W., Smith, F. T. & Walker, J. D. A. 1996 The onset of instability in unsteady boundary-layer separation. *J. Fluid Mech.* **315**, 223–256.

Cowley, S. J., Van Dommelen, L. L. & Lam, S. T. 1990 On the use of Lagrangian variables in descriptions of unsteady boundary-layer separation. *Phil. Trans. R. Soc. Lond.* A **333**, 343–378.

Degani, A. T., Li, Q. & Walker, J. D. A. 1996 Unsteady separation from the leading edge of a thin airfoil. *Phys. Fluids* **8**, 704–714.

Degani, A. T., Walker, J. D. A. & Smith, F. T. 1998 Unsteady separation past moving surfaces. *J. Fluid Mech.* **375**, 1–38.

Doligalski, T. L., Smith, C. R. & Walker, J. D. A. 1994 Vortex interactions with walls. *Annu. Rev. Fluid Mech.* **26**, 573–616.

Doligalski, T. L. & Walker, J. D. A. 1984 The boundary layer induced by a convected two-dimensional vortex. *J. Fluid Mech.* **139**, 1–28.

Elliott, J. W., Cowley, S. J. & Smith, F. T. 1983 Breakdown of boundary layers: (i) on moving surfaces; (ii) in semi-similar unsteady flow; (iii) in fully unsteady flow. *Geophys. Astrophys. Fluid Dyn.* **25**, 77–138.

Ghosh Choudhuri, P. & Knight, D. D. 1996 Effects of compressibility, pitch rate, and Reynolds number on unsteady incipient leading-edge boundary-layer separation over a pitching airfoil. *J. Fluid Mech.* **308**, 195–217.

Hoyle, J. M., Smith, F. T. & Walker, J. D. A. 1991 On sublayer eruption and vortex formation. *Comput. Phys. Commun.* **65**, 151–157.

Koumoutsakos, P. & Leonard, A. 1995 High-resolution simulations of the flow around an impulsively started cylinder using vortex methods. *J. Fluid Mech.* **296**, 1–38.

Lam, S. T. 1988 On high-Reynolds number laminar flows through a curved pipe and past a rotating cylinder. PhD dissertation, University of London.

Li, L., Walker, J. D. A., Bowles, R. I. & Smith, F. T. 1998 Short-scale break-up in unsteady interactive layers: local development of normal pressure gradients and vortex wind-up. *J. Fluid Mech.* **374**, 335–378.

Obabko, A. V. & Cassel, K. W. 2002 Detachment of the dynamic-stall vortex above a moving surface. *AIAA J.* to appear.

Obabko, A. V. 2001 Navier–Stokes solutions of unsteady separation induced by a vortex–comparison with theory and influence of a moving wall. PhD dissertation, Illinois Institute of Technology.

Orlandi, P. 1990 Vortex dipole rebound from a wall. *Phys. Fluids* A **2**, 1429–1436.

Peridier, V. J., Smith, F. T. & Walker, J. D. A. 1991*a* Vortex-induced boundary-layer separation. Part 1. The unsteady limit problem $Re \to \infty$. *J. Fluid Mech.* **232**, 99–131.

Peridier, V. J., Smith, F. T. & Walker, J. D. A. 1991*b* Vortex-induced boundary-layer separation. Part 2. Unsteady interacting boundary-layer theory. *J. Fluid Mech.* **232**, 133–165.

Seal, C. V., Smith, C. R., Akin, O. & Rockwell, D. 1995 Quantitative characteristics of a laminar, unsteady necklace vortex system at a rectangular block-flat plate juncture. *J. Fluid Mech.* **286**, 117–135.

Seal, C. V., Smith, C. R. & Rockwell, D. 1997 Dynamics of the vorticity distribution in endwall junctions. *AIAA J.* **35**, 1041–1047.

Sears, W. R. & Telionis, D. P. 1975 Boundary-layer separation in unsteady flow. *SIAM J. Appl. Maths* **28**, 215–235.

Smith, C. R. & Walker, J. D. A. 1995 Turbulent wall-layer vortices. In *Fluid Vortices* (ed. S. I. Green), pp. 235–290. Kluwer.

Smith, C. R., Walker, J. D. A., Haidari, A. H. & Sobrun, U. 1991 On the dynamics of near-wall turbulence. *Phil. Trans. R. Soc. Lond.* A **336**, 131–175.

Smith, F. T. 1988 Finite-time break-up can occur in any unsteady interacting boundary layer. *Mathematika* **35**, 256–273.

Van Dommelen, L. L. 1981 Unsteady boundary-layer separation. PhD dissertation, Cornell University.

Van Dommelen, L. L. & Shen, S. F. 1980 The spontaneous generation of the singularity in a separating laminar boundary layer. *J. Comput. Phys.* **38**, 125–140.

Van Dommelen, L. L. & Shen, S. F. 1982 The genesis of separation. In *Numerical and Physical Aspects of Aerodynamic Flows* (ed. T. Cebeci), pp. 293–311. Springer.

Walker, J. D. A. 1978 The boundary layer due to a rectilinear vortex. *Proc. R. Soc. Lond.* A **359**, 167–188.